Investigating genesis and early development of Arctic cyclones using an isentropic analysis
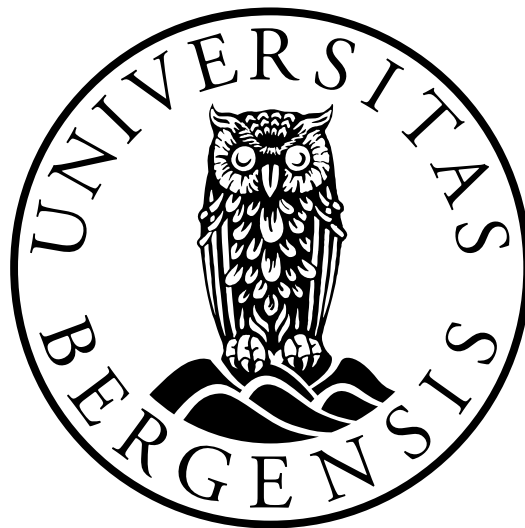
Andrea Rosendahl

Scientific environment

This study is carried out at the Geophysical Institute, University of Bergen. The work is part of the Nansen Legacy, an Arctic research project working on gaining knowledge on the climate and ecosystem in the Barents Sea. As part of the Nansen Legacy, I have attended conferences and discussed my thesis with other researchers, and I have learned about different aspects of the rapidly changing climate and ecosystem in the Arctic. I have also interacted with researchers in both the Climate Dynamics group at the Geophysical Institute and attended weekly meetings with the Storm Tracks group at Bjerknes Centre for Climate Research. Through these interactions, I have broadened my knowledge of the dynamics in the atmosphere and ocean.

Acknowledgements

First of all, I would like to thank my supervisors Camille Li and Dandan Tao. Thank you for providing such an interesting research opportunity, for all the help and for the interesting and engaging discussions along the way. I have learned a lot from you and have enjoyed working on this thesis.

I also would like to thank my fellow students and friends. Thanks for the fun coffee breaks and lunches, and all the trips we have done together. I hope there will be more! Doing this degree would not have been as fun without all of you.

Finally, I want to thank Vidar and my family for encouraging me and supporting me throughout this degree. Thanks for all the motivational pep talks, and also for reminding me that it is okay to relax. And to my grandpa, Peter Rosendahl, who was always so interested in what I was studying and knew so much, I wish you were here so I could discuss my master thesis with you.

Andrea Rosendahl
Bergen, 1st June 2024

Abstract

Cyclones are frequently found in the Arctic and can have wide-ranging impacts on the region. Nevertheless, few studies have focused on the development of cyclones originating in the Arctic, in contrast to the extensively studied midlatitude cyclones. Thus, in this thesis we study the genesis and development of cyclones originating in the Arctic. As these cyclones exhibit large variability in temperature and moisture content, we separate them into two groups - warm and moist cyclones versus cold and dry cyclones. This separation is based on the equivalent potential temperature θ_e, a quantity which is a function of temperature and humidity and is conserved for moist-adiabatic motion. The cyclones are tracked using the Melbourne tracking scheme on ERA5 reanalysis data, and we apply an isentropic framework to study the overturning circulation of the two groups. Cyclones in both groups show a thermally direct circulation, with higher θ_e (warm, moist) air rising and lower θ_e (cold, dry) air sinking. The high-θ_e cyclones have deeper but less vigorous overturning circulation compared to the low-θ_e cyclones. The circulations are most different at and just after cyclogenesis, and become more similar over time. Prior to cyclogenesis, the two groups show opposite atmospheric anomalies in the Arctic up to several days before the genesis event, suggesting that the environment is preconditioned. These atmospheric anomalies also exhibit a dipole pattern over the study region and North Atlantic, suggesting that the cyclones are related to large-scale systems such as jet and weather regimes. Further research on the connection between the two groups and the regimes is proposed. Different characteristics and genesis locations suggest that low-θ_e cyclones arise from baroclinicity from the sea ice edge while high-θ_e cyclones arise from other processes such as secondary genesis or orographic processes. Our results contribute to a better understanding of how thermodynamic characteristics of cyclones are connected to cyclone development and impacts on the Arctic region. Cyclones affect the local weather and can result in extreme warming, storm surges and flooding. Hence, knowing more about the development and impacts of cyclones can give more insight into how extreme cyclone events evolve.

Contents

List of Figures

Abbreviations

APE	Available Potential Energy
DJF	December, January and February
DLR	Downwelling Longwave Radiation
EA	East Atlantic pattern
NAO	North Atlantic Oscillation
NDJFM	November, December, January, February and March
P	Pressure
SDG	Sustainable Development Goals
SIC	Sea Ice Concentration
SLP	Sea Level Pressure
ΔQ	Heat Release
θ_e	Equivalent Potential Temperature

Chapter 1

Introduction

Extratropical cyclones are important for the climate system and determine many aspects of the surface weather. These weather systems are closed circulations where the wind blows around low-pressure centres in a counterclockwise direction in the Northern Hemisphere (*Wallace and Hobbs*, 2006). They can have a wide range of forms that depend on factors such as the moisture availability, the background flow, and characteristics of the surface underneath (*Wallace et al.*, 2006). In addition, cyclones may have a large impact on the environment through extreme winds, precipitation and temperatures, and sea ice melt and breakup (*Dacre and Pinto*, 2020). Such extreme events have great socioeconomic impacts on the cyclone region.

Cyclones are frequently found in the Arctic and affect the Arctic climate (*Walsh et al.*, 2018). The Barents Sea is the main corridor for cyclones entering the Arctic, with an average of 13 cyclones present in the Barents region per winter season, based on reanalysis data from 1979-2018 (*Madonna et al.*, 2020; *Tao et al.*, 2024). The cyclones transport warm and moist air poleward from the midlatitudes to the Arctic (*Sorteberg and Walsh*, 2008), causing the region to experience increased temperature and humidity. Further, cyclones travelling to the Arctic also affect the water transport variability into the Barents Sea, where more cyclones in the region (a lower atmospheric pressure) are associated with higher flows (more water moving past the area) (*Brown et al.*, 2023; *Heukamp et al.*, 2023). Thus, many cyclones found in the Arctic region are key contributors to both the atmospheric and oceanic environment.

As cyclones can have large impacts on the Arctic region, it is important to gain knowledge in how they affect the local climate, ecosystem, and communities. Cyclones contribute to most of the precipitation in the Arctic (*Hawcroft et al.*, 2012), and are associated with natural hazards close to the region, as they can cause very high winds, flooding, and storm surges (*Dacre and Pinto*, 2020; *Priestley et al.*, 2017). They can also lead to extreme events in the Arctic, such as the 2015/16 extreme warming event (*Binder et al.*, 2017; *Boisvert et al.*, 2016; *Madonna et al.*, 2020) and the January 2022 extreme sea ice melt event (*Blanchard-Wrigglesworth et al.*, 2022). According to climate models, the Arctic Ocean will be ice free in the summer by this century (*Stroeve et al.*, 2007), resulting in more seasonal ice that is both thinner and more vulnerable than multiyear ice. The Arctic will also likely experience more and longer winter warming events (*Graham et al.*, 2017), which may influence the frequency of extreme tempera-

tures, precipitation and sea ice melt. Studying the development and impact of cyclones will therefore contribute to the United Nations Sustainable Development Goals (SDG) 13, 14 and 15 (Climate action, Life below water and Life on land, respectively (*UN DESA*, 2023)), and can help the communities create better plans for climate mitigation and resilience.

Knowing more about the genesis and evolution of Arctic cyclones in general can help better appreciate how the extreme ones evolve. While there has been a lot of research on cyclones in the midlatitudes, less research has focused on the genesis and evolution of Arctic cyclones. It is recognised that the Arctic and the midlatitudes interact through air mass exchanges, and that the energy transport from the midlatitudes to the Arctic is important for the Arctic climate. However, questions are still present in how much midlatitude cyclone theory can be applied to Arctic cyclones (*Woollings et al.*, 2023), and what environmental conditions are important for development of these cyclones. To address these questions, this thesis explores the origin and development of Arctic cyclones.

1.1 Arctic Climate System

The Arctic is defined as the area north of 66° N and is mostly covered by ocean and ice. The region is typically very cloudy, with large seasonal and regional variations in temperature, and low mean annual winds and precipitation (chapter 2 in *Serreze and Barry*, 2005). In winter, there are large regional variations in the Arctic region. For example, the Siberian sector typically experiences weak winds and temperatures lower than -40° C, while the Atlantic sector experiences stronger winds and temperatures near 0° C. The largest amount of winter precipitation in the Arctic is also in the Atlantic sector (Figure 1.1). This is mainly due to large-scale precipitation (related to formation of synoptic clouds), while convective precipitation (related to mesoscale convection) accounts for less of the total precipitation. The climate in this region is strongly governed by both the northeastward extension of the primary North Atlantic storm track and the Icelandic low (chapter 2 in *Serreze and Barry*, 2005). The net precipitation over the Arctic Ocean contributes significantly to a very stable, stratified ocean with a low-salinity surface layer that inhibits vertical mixing. This fresh surface layer is maintained mainly by river input. Further, the Arctic Ocean varies greatly in depth, and is mostly covered by sea ice, with a maximum sea ice cover in March and minimum sea ice cover in September. In winter, the Barents Sea has less sea ice cover and thus more open ocean than other sectors of the Arctic Ocean.

The atmosphere, ocean and land in the Arctic climate system are closely connected through energy transfer between the components (chapter 2 in *Serreze and Barry*, 2005). The Arctic experiences an annual-mean energy imbalance, with a net deficit of energy due to more outgoing longwave radiation than incoming solar radiation (*Hartmann*, 2016). This energy imbalance is partly reduced by the import of energy from lower latitudes, both by the atmosphere and the ocean. The sea ice has a high albedo and reflects incoming solar radiation, while the ocean has a low albedo and absorbs most of the incoming solar radiation. The turbulent fluxes exchange energy between the ocean
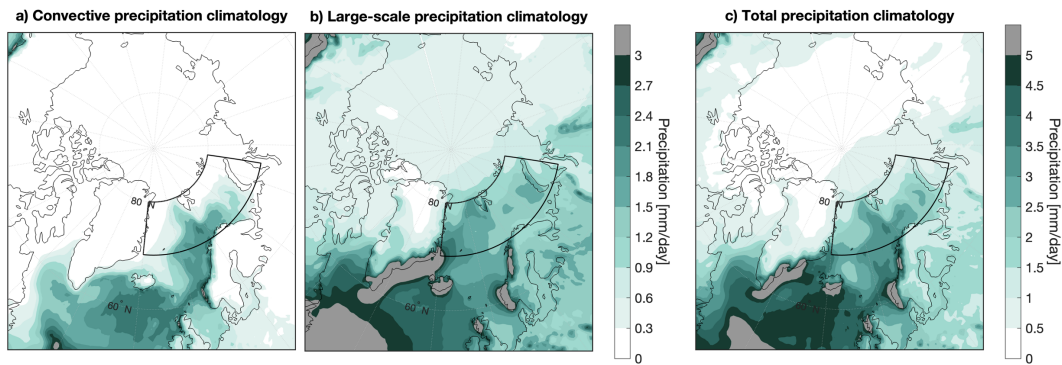
Figure 1.1: Precipitation climatology for the extended winter season (November to March, NDJFM) in the Arctic region. The precipitation [mm/day] can be split into a) convective and b) large-scale precipitation, where the sum is c) total precipitation. Grey shading indicates any values above 3 mm/day (a,b) or 6 mm/day (c). The study region is indicated by the black contour.

and the atmosphere, both through evaporation (latent heat flux) and thermal conduction (sensible heat flux). In winter, the difference between incoming and outgoing radiation is at its greatest, with the incoming solar irradiance being almost negligible. The turbulent fluxes are therefore greatest in winter and are mostly negative, indicating a transfer of energy from the ocean to the atmosphere (Figure 1.2). While the latent heat flux is always negative over the ocean (water always evaporates from the ocean to the atmosphere), the sensible heat flux is slightly positive over Greenland, due to the cold surface of the Greenland ice sheet compared to the atmosphere. The strongest turbulent fluxes in the Arctic are found in the Atlantic sector (region marked by black contour line), displaying strong transfers of energy from the ocean to the atmosphere. Here, the average turbulent heat flux in winter is -93.3 W/m^2, while in the whole Arctic the average turbulent heat flux in winter is only -11.9 W/m^2. This is because of the large area of sea ice, covering the ocean and reducing the heat transfer between ocean and atmosphere.

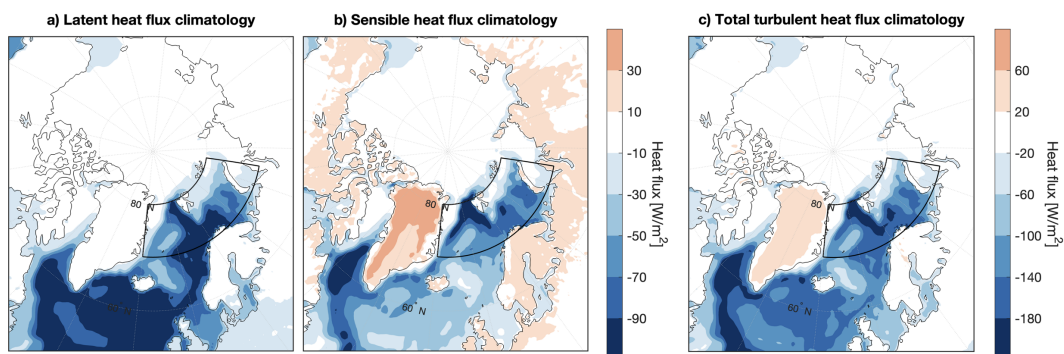*Figure 1.2: Turbulent heat flux climatology for the extended winter season (November to March, ND-JFM) in the Arctic region. The turbulent heat flux [W/m^2] can be split into a) latent and b) sensible heat flux, where the sum is c) total turbulent heat flux. Positive (negative) values indicate heat fluxes from the atmosphere (ocean) to the ocean (atmosphere). The study region is indicated by the black contour.*

1.2   Cyclone impacts in the Arctic

Cyclones transport heat and moisture into the Arctic, potentially affecting the local climate in the region through changes in temperature, energy budget, sea ice and permafrost. They account for 74% of the annual poleward moisture flux across 70° N, and are closely linked to extreme wintertime moisture transport events into the Arctic (*Fearon et al.*, 2021; *Papritz and Dunn-Sigouin*, 2020). An increase in moisture may enhance the downwelling longwave radiation that can lead to surface warming (*Boisvert et al.*, 2016; *Messori et al.*, 2018). The outgoing longwave radiation can also increase from higher air temperatures due to cyclones, whereas increasing surface turbulent fluxes are mainly dominated by the strong winds, as the strength of the turbulent fluxes depends on wind speed (*Blanchard-Wrigglesworth et al.*, 2022). High temperatures and humidity due to cyclones can also cause sea ice melt from the enhanced downwelling longwave radiation (*Boisvert et al.*, 2016; *Mortin et al.*, 2016), and an increased moisture transport into the Arctic during winter is key for melt onset (*Papritz and Dunn-Sigouin*, 2020). Further, the winds from cyclones can cause sea ice breakup and sea ice export (*Sorteberg and Kvingedal*, 2006). Hence, cyclones can affect the local climate both thermodynamically (temperature and moisture) and dynamically (wind).

The impact of a cyclone in the Arctic depends on its development and characteristics, and hence, varies across different cyclones. The exact location and path of the cyclone matter for the impacts, but also the placement of the fronts that separate the cyclone's warm and cold sectors (chapter 10 in *Hakim and Patoux*, 2018). For example, these details of the cyclone's structure may be linked to sea ice changes in the Arctic-Atlantic sector over the last 20 years (*Aue et al.*, 2022). While the warm sector in front of the cyclones caused a sea ice reduction in the Greenland Sea prior to cyclone passage, the cold sector behind the cyclones caused a sea ice increase in the Barents Sea after cyclone passage. In addition, *Madonna et al.* (2020) discovered that it is not necessarily the cyclones with the deepest central low-pressures that result in the largest impacts. Instead, the cyclone-induced surface warming in the Barents region depends mainly on the cyclone's origin, where cyclones originating in the North Atlantic are associated with a stronger warming compared to cyclones originating north of 60° N.

Cyclone variability is closely connected to large-scale atmospheric conditions. Months with many cyclones present in the Barents Sea are characterised by strong upper-level winds and a southwest-northeast tilted jet that can influence where the cyclone travels by facilitating a pathway to the Arctic (*Madonna et al.*, 2020; *Shaw et al.*, 2016). Different jet modes are linked both to different large-scale flow regimes in the North Atlantic and to cyclone frequency in the Arctic, where specific jet modes are connected to a preconditioning of the Arctic for cyclogenesis and growth (*Madonna et al.*, 2017; *Tao et al.*, 2024). Cyclone frequency may also depend on atmospheric blocking (persistent anticyclones lasting a week or more), as blocking can divert the North Atlantic storm track and cause a poleward transport of cyclones (*Binder et al.*, 2017; *Madonna et al.*, 2020). Consequently, atmospheric blocking location, large-scale flow regimes and the jet stream can all affect cyclone path and frequency.

1.3   A warming Arctic

Under global warming, the Arctic is warming faster than the rest of the world, a phenomenon known as Arctic Amplification (chapter 2 in *Serreze and Barry*, 2005). The Arctic is projected to experience higher temperatures and reduced sea ice cover, as well as an increased precipitation variability due to increasing variability of poleward moisture transport into the Arctic (*Bintanja et al.*, 2020). Also, the Arctic land-sea temperature contrast in the summer has strengthened and the sea ice cover has reduced markedly over the reanalysis period (*Day and Hodges*, 2018; *Serreze et al.*, 2007). By the year 2100, the Arctic Ocean is projected to be ice free in September (*Boé et al.*, 2009; *Stroeve et al.*, 2007). Thus, Arctic warming is already evident, highlighting the importance of further research on this region.

Arctic Amplification may cause changes in storm track location or intensity, thus affecting the number of cyclones reaching the Arctic. The storm track location can be influenced by several different mechanisms (*Shaw et al.*, 2016). For example, a decreasing equator-to-pole gradient in the lower troposphere can cause an equatorward shift of the storm track, while a warming of the tropical upper troposphere will shift the storm track poleward (*Butler et al.*, 2010; *Catto et al.*, 2011). The opposing effects and the uncertainties in changes of the temperature gradient make predicting the storm track movement challenging, but there is an emerging consensus that, under strong greenhouse forcing, the storm track (and the jet) will move poleward (*Harvey et al.*, 2015; *Shaw et al.*, 2016). These changes in jet and storm track position affect where cyclones travel and can therefore influence the local climate, for example by a change in the amount of precipitation and wind strength (*Bengtsson et al.*, 2006). In addition, sea ice reduction increases the heat and moisture in the atmosphere and can therefore affect the atmospheric circulation and stability, which can further affect cyclone frequency, intensity and, according to some studies, path (*Catto et al.*, 2011; *Hay et al.*, 2023; *Inoue et al.*, 2012; *Koyama et al.*, 2017). Also, the change in cyclone frequency and path influences the poleward heat and moisture transport by the cyclones into the Arctic region (*Hartmuth et al.*, 2023).

1.4   Research questions

While *Madonna et al.* (2020) found that cyclones originating in the Arctic on average have a weaker impact on the region compared to North Atlantic cyclones, *Tao et al.* (2024) discovered that cyclones originating in the Arctic exhibit large variability in their temperature and moisture content (see Section 3.4). We therefore want to investigate if the warm and moist cyclones are different from the cold and dry cyclones. Based on this, my research questions are:

- Do warm and moist cyclones exhibit a different dynamical development from cold and dry cyclones?

- What are the differences in the energy cycle of warm and moist cyclones compared to cold and dry cyclones?

- Do warm and moist cyclones and cold and dry cyclones have different impacts on the Arctic region?

To answer these questions, I will use a framework that is well suited for studying the overturning circulation of cyclones. Using this framework, I will look at the genesis and early development of the overturning circulation connected to the warm and moist cyclones and the cold and dry cyclones originating in the Arctic.

1.5   Thesis outline

Chapter 1 gives a broad overview of the motivation and background for this thesis. Chapter 2 includes more detailed information about Arctic cyclones, while Chapter 3 discusses the methodology. The results are presented in Chapter 4, with a wider discussion in Chapter 5. A final conclusion is presented in Chapter 6.

Chapter 2

Arctic Cyclones

Extratropical cyclones originating in the midlatitudes can be described by the Norwegian polar front cyclone model, with a strong cold front, a weaker occluded front, and a comma-shaped cloud shield (*Bjerknes*, 1919; *Bjerknes and Solberg*, 1922; *Wallace et al.*, 2006). These extratropical cyclones differ from the more axially symmetric tropical cyclones, as they tend to be shorter-lived and are generally larger in scale compared to the tropical cyclones. Further, extratropical cyclones are frequently found in the Arctic region. Between 1979-2020, 1280 cyclones were present in the Arctic (Figure 2.1a), where 299 cyclones arrived in the extended Barents region (hereafter called the study region, see Section 3.1) from the south, 31 cyclones arrived in the study region from the north, 378 had genesis in the study region, and 572 were present in the Arctic but never reached the study region (Table 2.1b). Most of the cyclones present in the Arctic are connected to the extended North Atlantic storm track (chapter 4 in *Serreze and Barry*, 2005), which is an area of strong eddy kinetic energy mainly due to transient eddies (fluxes that deviate from both time-mean and zonal-mean), i.e., cyclones and anticyclones (chapter 5 in *James*, 1994). For the rest of the thesis, we use the term cyclones when referring to extratropical cyclones.

Several processes are needed for cyclones to originate and develop. They are created from sources of baroclinic instability, which requires a horizontal temperature gradient (chapter 9 in *Vallis*, 2017). Baroclinic instability arises from vertical shear in the jet stream, i.e., a change in wind strength with height. The vertical shear connects to the horizontal temperature gradient through the thermal wind balance (chapter 14 in *Hoskins and James*, 2014), given by:

$$\frac{\partial V_g}{\partial z} = \left(\frac{R}{f} \ln \frac{p_1}{p_2} \right) \mathbf{k} \times \nabla \overline{T} \qquad (2.1)$$

where $\frac{\partial V_g}{\partial z}$ is the vertical shear of the geostrophic wind, R is the gas constant for air, f is the Coriolis parameter, p_1 and p_2 are the pressures at the top and bottom of the layer, and $\nabla \overline{T}$ is the horizontal temperature gradient with $\overline{T}$ as the vertically averaged temperature for the layer. For the cyclone to develop, both a lower-level and an upper-level gradient need to be present. A lower-level meridional temperature gradient naturally exists because of the Equator-to-pole temperature difference (chapter 9 in *Vallis*, 2017). The lower-level baroclinicity can be measured by the Eady growth rate, which estimates the growth of baroclinic instability (*Eady*, 1949). In the upper-level, troughs

Cyclones present in the Arctic

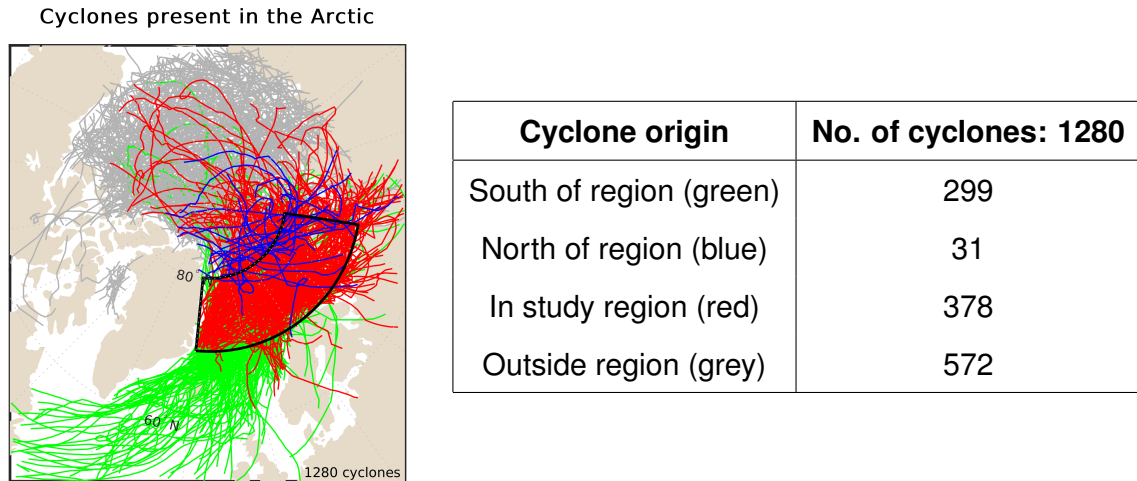| Cyclone origin	No. of cyclones: 1280
South of region (green)	299
North of region (blue)	31
In study region (red)	378
Outside region (grey)	572

Figure 2.1: Cyclones present in the Arctic during DJF winter in ERA5 reanalysis (1979-2020). (left) Map of the paths for all cyclones, colour-coded by origin. Black contour shows the study region, see Section 3.1. (right) Number of cyclones in each group. A total of 1280 cyclones are present in the Arctic during this period. 299 cyclones reach the study region from the south (green), 31 cyclones reach the study region from the north (blue) and 378 cyclones have genesis inside the study region (red). 572 cyclones are present in the Arctic but do not enter the study region (grey).

of low pressure in the jet stream can result in a potential vorticity anomaly inducing circulation that extends downward towards the surface and causes the surface pressure to fall (chapters 10 in *Hakim and Patoux*, 2018; *Holton*, 2004). The upper-level gradient needs to be tilted westward with respect to the lower-level gradient for the cyclone to grow. As the cyclone grows, this tilt eventually becomes vertical or eastward tilted, and the cyclone will start to decay.

Cyclones and large-scale flow interact with each other. Large-scale flow influences where the cyclones form, as meridional circulations in the jet entrance and exit regions create cyclonic vorticity and thus a foundation for cyclogenesis (chapter 5 in *James*, 1994). Movement of the jet may displace the storm track, as the storm track is most intense on the poleward side near the jet exit, therefore affecting the location of cyclogenesis. The location of cyclogenesis and cyclone pathway may also be influenced by other large-scale atmospheric flows, such as blocks (*Madonna et al.*, 2020). A block is a persistent anticyclone lasting longer than a week, where an anticyclone is a high-pressure area with almost no wind or cloud formation close to the centre, and with wind moving around the area in a clockwise manner in the Northern Hemisphere (chapter 10 in *Hakim and Patoux*, 2018). Blocks may prevent the eastward motion of cyclones, and instead steer the cyclones poleward towards the Arctic region (chapter 5 in *James*, 1994). Moreover, transient eddies can also influence the large-scale flow, as the eddies accelerate the jet and cause westerly acceleration in the midlatitudes (chapter 14 in *Hoskins and James*, 2014). Further, cyclones and travelling anticyclones can reinforce and maintain a block, while an intense cyclone may be able to disrupt the block (chapter 5 in *James*, 1994). The interactions between the large-scale flow and cyclones may therefore affect frequency, location, and path of Arctic cyclones.

Cyclones link to the general circulation through the Lorenz energy cycle, as they con-

vert available potential energy (APE) to kinetic energy (chapter 5 in *James*, 1994). APE exists from tilted isentropes (lines of constant equivalent potential temperature, Section 3.3) due to the temperature gradient between the Equator and the pole. A larger tilt of the isentropes mean that the eddies can convert more APE to kinetic energy, which influences the energy cycle. The Lorenz energy cycle gives an overview of the dominant processes in the atmosphere that give rise to motions, and includes several steps (chapter 10 in *Holton*, 2004; *Lorenz*, 1955). First, zonal APE is created from heating near the Equator and cooling near the pole. Next, zonal APE converts into eddy APE as the transient eddies transport warm air poleward and cold air equatorward. This horizontal transport of warmer and colder air causes vertical motions in the eddies, transforming some of the eddy APE to eddy kinetic energy. Lastly, the eddy kinetic energy converts into zonal kinetic energy by the momentum fluxes. The Lorenz energy cycle therefore shows the importance of the transient eddies, which contribute markedly to the large-scale poleward transport of heat in the Northern Hemisphere as they transport momentum, energy, and potential vorticity between lower and higher latitudes (chapters 16 and 5 in *Hoskins and James*, 2014; *James*, 1994, respectively).

Cyclones generally result in clouds and precipitation, where the release of latent heat of condensation influences the energy connected to the cyclones (*Wallace et al.*, 2006). The latent heat of condensation is the heat that releases when water changes from vapour to liquid. It occurs mostly in warm and rising air, increasing the tilt of isentropes and therefore the amount of APE that can convert to kinetic energy. The moisture in cyclones can therefore influence the amount of energy in the Lorenz energy cycle that is connected to the cyclones. In addition, cyclones and blocks exhibit a strong link with the local moisture transport, where cyclones favour a net moisture transport and blocks favour a total moisture transport into the Arctic (*Papritz and Dunn-Sigouin*, 2020). This relates to the baroclinic vertical structure found in cyclones compared to the more barotropic structure in blocks, where increasing APE from increased moisture creates a foundation for baroclinic instability to form. Thus, it is important to consider the moisture content of cyclones when studying cyclone energy and impact.

Extratropical cyclones can frequently originate in the Arctic, partly because of orographic effects from Greenland and partly because of enhanced baroclinicity along the sea ice edge (chapter 4 in *Serreze and Barry*, 2005). These cyclones can affect the Arctic climate by causing increased winds and temperatures, sea ice melt and potentially flooding (*Dacre and Pinto*, 2020). Hereafter, we define Arctic cyclones as cyclones with genesis in the Arctic region, i.e., originating north of 66° N, as they are the target cyclones of this thesis.

Chapter 3

Data & Methods

3.1 Data

This thesis uses European Centre for Medium-Range Weather Forecasts (ECMWF) re-analysis data ERA5 (*Hersbach et al.*, 2023) for information on the atmospheric and surface environment to study the Arctic cyclones. As observations are unevenly distributed across the globe, we use reanalysis data, which is a global dataset created by the laws of physics and is constrained by most of the available observations through data assimilation. The data used is 3-hourly spaced on 19 vertical pressure levels, on a regular latitude-longitude grid with 0.25° spacing. We use the variables temperature T $[K]$, specific humidity q $[g/kg]$, vertical velocity w $[m/s]$ and pressure P $[hPa]$ for the isentropic analysis (see Section 3.4). For additional analysis, we look at horizontal velocities u and v $[m/s]$, sea level pressure SLP $[hPa]$, precipitation (total tp, large-scale lsp and convective cp) $[mm/day]$, downwelling longwave radiation DLR $[W/m^2]$, turbulent heat fluxes (total $hflux$, sensible $hfss$ and latent $hfls$) $[W/m^2]$, total snowfall tsf $[mm/day]$, and sea ice concentration SIC $[-]$.

Following the method in *Tao et al.* (2024), we focus on the Arctic cyclones with genesis within our study area: 70° to 80° North and -20° to 70° East. This area is the Atlantic gateway into the Arctic Ocean, which includes the Barents Sea, the Greenland Sea and parts of the Norwegian Sea. The data period is 1979-2020 and only cyclones with genesis during the winter months (December, January, and February (DJF)) are included in the analysis. As some of the cyclones are at the start or end of the winter season, we also include the months November and March (NDJFM) in an extended winter season when calculating climatology and 9-day evolutions for the cyclones. We study the winter season as this is when the surface baroclinicity is the strongest, making the winter cyclones generally more intense (*Chang et al.*, 2002). To account for the rapid Arctic warming during the study period, we remove the long-term trend from the data, by fitting a quadratic function to the monthly data.

3.2 Cyclone tracking

There are many ways to identify and track extratropical cyclones (*Neu et al.*, 2013). While all the tracking methods agree on the major cyclone activity areas and spatial

structures, other factors of cyclone tracking are more sensitive to the method. For example, the tracking methods agree more for winter cyclones than summer cyclones. The tracking can be based on different atmospheric variables, where the most common tracking methods either use local mean SLP minima or use vorticity maxima at a specific pressure level (*Walker et al.*, 2020). The tracking of short-lived cyclones exhibits the largest spread between methods, and the differences between the SLP and vorticity methods are most apparent at the start and final stages of the tracks (*Neu et al.*, 2013; *Walker et al.*, 2020).

The cyclone tracks in this thesis are identified and tracked by the Melbourne tracking scheme, which locates and tracks the cyclones using mean SLP analyses (*Simmonds and Murray*, 1991a). First, the scheme locates spatially where the Laplacian of pressure is at a local maximum, which is used as a starting point. Next, based on this starting point, the scheme searches for a pressure minimum in close vicinity. This is the position of the cyclone at the first time step. To get the position of the cyclone at the next time step, the scheme uses weighting to combine cyclone path tendency and the pressure map to estimate the highest probability of where the next pressure minimum will be. In this manner, the cyclones are tracked from cyclogenesis to cyclolysis, giving the whole lifespan of the cyclone. The scheme also includes open depressions, as they may help maintain the continuity of the tracks. To exclude heat lows and insignificant cyclonic features, the scheme contains a criterion of a minimum value of the Laplacian of pressure around the depression centre (*Simmonds and Murray*, 1991b). In addition, for this thesis, an extra criterion of a minimum lifespan of 48 hours for the tracks has been included to exclude polar lows (*Michel et al.*, 2018). This results in a dataset containing all cyclone tracks that are 48 hours or longer, with information about the tracks from cyclogenesis to cyclolysis.

There are some limitations and uncertainties connected to tracking cyclones using the Melbourne scheme. Generally, latitude-longitude grids may have problems with tracking through space, as the grid box sizes decrease with higher latitudes (*Walker et al.*, 2020). The accuracy of the individual cyclone track is not always guaranteed, as the tracks are estimated based on statistical calculations (*Simmonds and Murray*, 1991a). Further, local and daily variations in cyclone movement and frequency can result in an overestimated number of cyclogenesis and cyclolysis, and truncated tracks. As the Melbourne scheme includes open depressions, this overestimation is, however, somewhat reduced.

3.3   Variability of cyclone characteristics

One way of studying the thermodynamic characteristics of the cyclones is to use the potential temperature. Potential temperature θ $[K]$ is the temperature an air parcel would have if it was brought adiabatically (no heat exchange with the environment) to a reference pressure. It is given by:

$$\theta = T * \left(\frac{p_0}{p_d}\right)^{\frac{R_d}{C_p}} \tag{3.1}$$

where T is temperature, p_d is pressure, $p_0 = 1000\,hPa$ is the reference pressure, $R_d = 287.058\,J/kgK$ is the gas constant of dry air and $C_p = 1003.5\,J/kgK$ is the specific heat of air. Potential temperature is conserved in adiabatic flow, and changes only in the presence of diabatic effects (chapters 6 and 1 in *Hoskins and James*, 2014; *Vallis*, 2017, respectively). Its vertical gradient governs the dry static stability of the atmosphere, where an increasing potential temperature with height means that the dry atmosphere is stable (*Hartmann*, 2016).

As moisture is an integral part of cyclone thermodynamics, we also need to take this into account and therefore use equivalent potential temperature, $\theta_e\;[K]$. Following equation (2) in *Pauluis and Mrowiec* (2013), θ_e is given by:

$$\theta_e = T * (\frac{p_0}{p_d})^{\frac{R_d}{C_p}} exp(\frac{L_v r}{C_p T}) H^{\frac{-R_v r}{C_p}}$$

(3.2)

where $R_v = 461.495\,J/kgK$ is the gas constant of water vapour, $L_v = 2.501 * 10^6\,J/kg$ is the latent heat of vaporisation, H is the relative humidity and r is the mixing ratio for water vapour. θ_e is the temperature an air parcel would have if it was first brought moist-adiabatically to 0 hPa until all moisture is condensed, and then brought adiabatically down to a reference pressure (*Hartmann*, 2016). As it is conserved in adiabatic processes with the presence of water phase change, it is a better representation of a moist atmosphere than the potential temperature (*Fang et al.*, 2017). An air parcel moving towards a lower θ_e will indicate that the air parcel becomes drier and/or colder. Further, in a thermally direct circulation, rising air has a higher θ_e compared to descending air, meaning warm and moist air rises and cold and dry air sinks (*Mrowiec et al.*, 2016). θ_e can therefore act as a representation of the thermodynamic characteristics of air parcels.

As Arctic cyclones exhibit large variability in temperature and moisture, we categorise the cyclones based on their thermodynamic characteristics to study this variability (Figure 3.1). The cyclones with the 10% highest and 10% lowest θ_e (named high-θ_e (red) and low-θ_e (blue), respectively) are chosen based on the mean θ_e of each cyclone. The mean θ_e is calculated at cyclone genesis, averaging over a 500 km radius circle around the cyclone centre in the horizontal and over pressure levels 1000-850 hPa in the vertical. The two groups are markedly different in θ_e, as well as T and q (Figure 3.1b,c), with a larger difference close to the surface (by definition of the two groups) and a smaller difference further up in the troposphere. After closer investigation of the SLP evolution of each cyclone, some cyclones have been excluded from the groups as they have their lowest SLP at the end of their life cycles, meaning the tracks end when the cyclones are the strongest. The high-θ_e group therefore consists of 35 cyclones while the low-θ_e group consists of 29 cyclones (see Appendix A).

3.4 Isentropic Analysis

Studying cyclone development in the conventional Eulerian framework (x,y,z direction) is complicated due to the complex structure of the cyclones and the surrounding area. Consider an example of a cyclone at genesis (Figure 3.2). The wind moves in a counterclockwise direction around the cyclone centre and has a clear change in wind
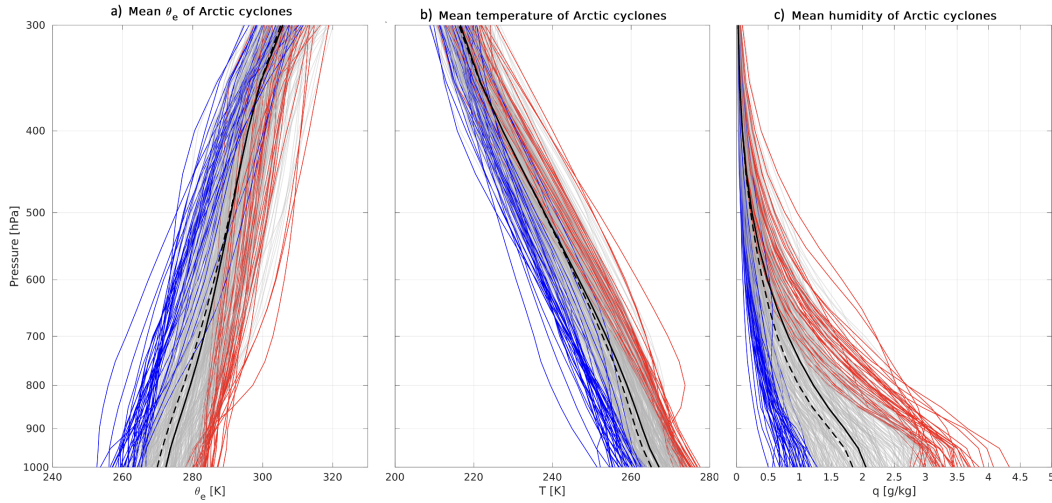
Figure 3.1: Vertical profiles of key characteristics of cyclones with genesis in the study area during DJF winter in ERA5 reanalysis (1971-2020). a) Equivalent potential temperature θ_e [K], b) temperature T [K] and c) humidity q [g/kg] averaged over a 500-km radius from the cyclone centre. Cyclones in the high-θ_e group (red) and low-θ_e group (blue) are defined in Section 3.3. The average cyclone profile is given by the solid black line, while the climatological profile is given by the dashed line.

direction along two "bulges" in the SLP contour surrounding the centre, indicating the location of the warm (red line east of cyclone) and cold (blue line south-southwest of cyclone) fronts (Figure 3.2a). In between the two fronts, there is a clear warm sector to the southeast of the cyclone, while the cold sector is located outside the fronts. As the atmospheric environment changes along with the cyclone movements, we need to follow the cyclone as it travels to study the cyclone evolution, which is an intricate process. The energy related to cyclones is connected to the vertical circulation (from release of APE, see Chapter 2), and we therefore need to consider the rising and sinking warm and cold air. This can be shown by the vertical velocity (Figure 3.2b), which is a messy structure with many small patches of positive and negative vertical velocities surrounding the cyclone centre. Determining the vertical circulation based on this messy structure will therefore be difficult. In addition, studying the vertical circulation of cyclone composites requires to centre and stack each of the cyclones based on the front locations, to make sure the warm rising air and cold sinking air are treated separately. Studying the vertical circulation of cyclones using another framework that simplifies the analysis of this complex structure is therefore preferred.

Pauluis et al. (2008) introduced the isentropic framework that can be used to investigate air parcel transport and energy cycles, and gives a simple representation of the vertical motions. The meridional isentropic framework (y,θ_e,p,t) can be formed by coordinate transformation from the conventional Eulerian framework (x,y,z,t), and provides a new perspective on air parcel trajectory compared to the Eulerian circulation. For example, the meridional circulation in the isentropic framework has one single overturning cell from the Equator to the pole in each hemisphere, while the Eulerian circulation has three overturning cells in each hemisphere (Figure 3.3) (*Pauluis and Mrowiec*, 2013). As the total mass flux is poleward, this agrees with the single overturning cell in the isentropic framework, but not the thermally indirect Ferrel cell in the Eulerian circula-
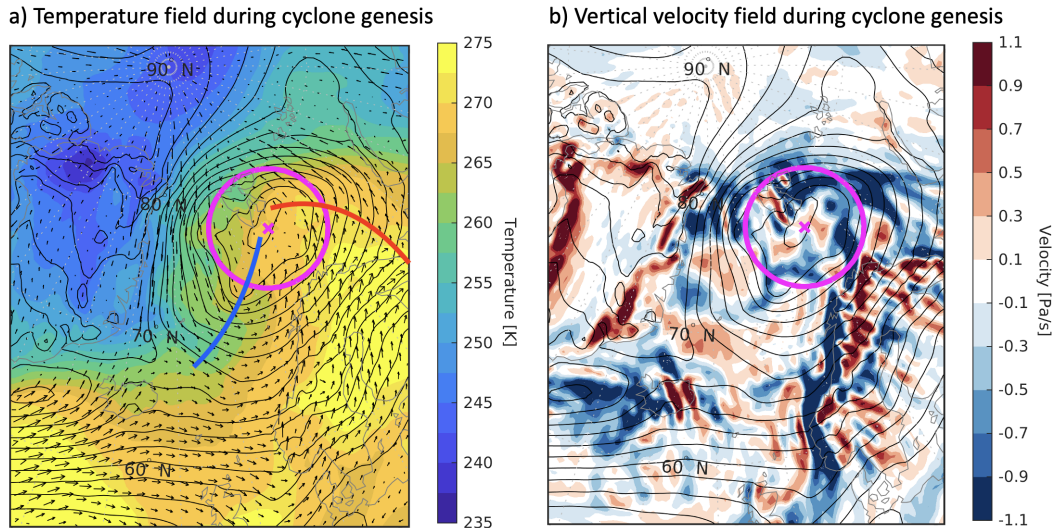
Figure 3.2: The atmospheric environment at 850 hPa during cyclogenesis for an Arctic cyclone with genesis in DJF winter, shown by a) temperature [K] (shading) and horizontal wind velocity [m/s] (arrows) and b) vertical wind velocity [m/s] (shading). The pink x denotes the centre of the cyclone at genesis, with a pink circle denoting the area enclosed within a 500 km radius around the cyclone centre. The red (blue) line represents the warm (cold) front. Sea level pressure (SLP) is shown by the black contours.

tion (chapter 15 in *Vallis*, 2017). While the Eulerian framework is good when studying air parcel movement, the isentropic framework is better when studying the energy cycle. Considering the vertical circulation in the isentropic framework, the horizontal coordinates can be compressed into the thermodynamic coordinate, reducing the number of dimensions to a (θ_e,p,t) framework (*Pauluis and Mrowiec*, 2013).

The isentropic framework is well-suited for studying energy conversion and vertical circulation. For example, this framework has previously been used on tropical cyclones (e.g., *Fang et al.*, 2017; *Pauluis and Mrowiec*, 2013). Moist isentropic surfaces are surfaces of constant θ_e and are conserved for reversible moist adiabatic processes. An air parcel crossing an isentropic surface will therefore indicate that some amount of heat has been added or removed from the system. Additionally, the framework gives information on the circulating mass transport without having to separate the vertical circulation and the surrounding environment, as it splits the air parcels into warm and moist ascending air and cold and dry descending air. The area of the thermally direct circulation (warm air rises while cold air sinks) gives the energy release connected to this circulation. Further, the isentropic framework separates the vertical circulating motions from the unwanted reversible oscillations, such as gravity waves. The framework is therefore a robust method in characterising the energy and thermodynamic properties of the updrafts and downdrafts in a vertical circulation.

The isentropic framework groups the air parcels based on their θ_e and adds each group together at each vertical level for each θ_e value (*Pauluis and Mrowiec*, 2013). This creates an overview of the amount of air parcels with a specific θ_e, shown in thermodynamic space. To compensate for the coarse horizontal resolution of the ERA5 dataset
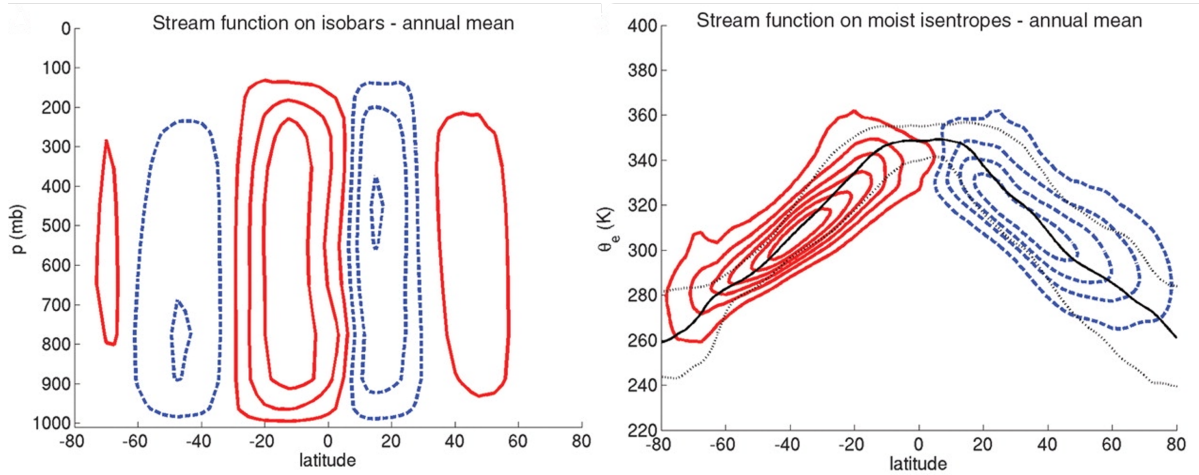
Figure 3.3: Differences in the global meridional circulation patterns between the conventional Eulerian coordinate system that uses pressure levels as the vertical component (y, P) (left) and the moist isentropic coordinate system that uses θ_e as the vertical component (y, θ_e) (right). The Eulerian coordinate system has three overturning cells in each hemisphere, while the isentropic coordinate system only has one overturning cell in each hemisphere. Figure retrieved from Pauluis et al. (2008).

and get a clearer result from the isentropic analysis, we apply a running mean of 12 hours. The earliest result is therefore at 6 hours after genesis, i.e., the average of 0-12 hours after genesis.

After grouping the air parcels, we can study the isentropic circulation by calculating the vertical mass flux $\rho w \ [kg/m^2 s]$. Following *Pauluis and Mrowiec* (2013), the mass flux is given by:

$$\langle \rho w \rangle (z, \theta_{e0}, t) = \iint_A \rho(x, y, z, t)[w(x, y, z, t) - \overline{w}(z, t)] \delta\{\theta_{e0} - \theta_e(x, y, z, t)\} dx dy \quad (3.3)$$

where ρ is the air density, w is the vertical velocity, $\overline{w}$ is the vertical velocity averaged over the entire domain A, and δ is the Dirac delta function that is either 0 or 1 depending on the difference between θ_e and a specific θ_{e0} value. The isentropic mass flux includes the vertical velocity relative to the surrounding environment, and describes the properties of the rising and sinking air parcels (*Fang et al.*, 2017; *Pauluis and Mrowiec*, 2013). Consider the mass flux of the same cyclone that we studied in Eulerian coordinates (Figure 3.4a). The positive values (red) indicate upward motion while the negative values (blue) indicate downward motion, displaying a thermally direct motion of rising higher θ_e air and subsiding lower θ_e air. The width of the mass flux area indicates the temperature differences between the rising and sinking air, and the height of the mass flux area indicates the depth of the circulation (*Mrowiec et al.*, 2016).

The isentropic circulation can also be visualised by integrating the mass flux to get the isentropic streamfunction $\Psi \ [kg/s]$. Following *Pauluis and Mrowiec* (2013), the streamfunction is given by:

$$\Psi(z, \theta_e, t) = \int_{-\infty}^{\theta_e} \langle \rho w \rangle (z, \theta_e, t) \, d\theta_e \quad (3.4)$$

The streamfunction represents the vertical circulation in a simple way, as it specifies the total upward mass transport of all air parcels with a θ_e lower or equal to a specific θ_e value at each pressure level (*Mrowiec et al.*, 2016). The mean flow of the air parcels in isentropic coordinates occurs along constant values of streamfunction, called streamlines, and moves clockwise around increasing streamfunction values and counterclockwise around decreasing values (*Pauluis and Mrowiec*, 2013). Figure 3.4b shows the streamfunction of the same cyclone as previously considered. The mean flow is counterclockwise, indicating a thermally direct circulation, consistent with the mass flux. Mixing of the air parcels with the surrounding environment, called entrainment, affects the θ_e of the air parcels. Thus, nearly vertical streamlines (minimal changes in θ_e) indicate little to no entrainment while nearly horizontal streamlines (large changes in θ_e) indicate strong entrainment or surface fluxes (*Pauluis and Mrowiec*, 2013).
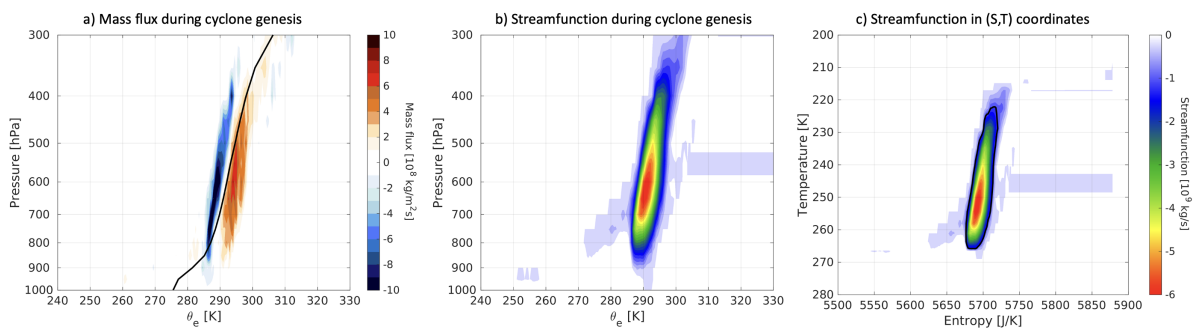
Figure 3.4: Isentropic framework during cyclogenesis for an Arctic cyclone with genesis in DJF winter. a) Isentropic mass flux $[kg/m^2 s]$, with positive (negative) values indicating ascending (descending) motion. b) Isentropic streamfunction $[kg/s]$, with decreasing values towards the centre indicating a counterclockwise movement of air parcels along the streamlines (constant streamfunction magnitude). c) Isentropic streamfunction $[kg/s]$ transformed to (S,T) coordinates, with the black contour indicating the streamfunction value of $-1*10^9 kg/s$.

The "area" covered by the streamfunction gives an estimate of the amount of heat that is released by the overturning circulation. Following *Fang et al.* (2019), the heat release $\Delta Q \, [J]$ is given by:

$$\Delta Q = \int T dS \qquad (3.5)$$

where dS is change in entropy $[J/K]$ (degree of disorder in the system). ΔQ is also affected by the Gibbs free energy, but as this term is small (*Fang et al.*, 2019), we have chosen to neglect it. To calculate the heat release, we first transform the streamfunction from (θ_e, P) coordinates to (S,T) coordinates (Figure 3.4c). The temperature T is calculated by taking the mean temperature at each pressure level. The entropy is given by:

$$S = C_p * ln\theta_e \qquad (3.6)$$

Finally, we integrate equation 3.5 along a selected streamfunction value of $-1*10^9 kg/s$ in (S,T) space (black contour in figure), such that we include most of the streamfunction. This gives us the area inside this streamline and, thus, the heat release ΔQ. ΔQ indicates the change in energy during the evolution of the cyclone, and is related to the kinetic energy and thermodynamic cycle of the cyclone.

Chapter 4

Results

4.1 Arctic cyclones with low-θ_e and high-θ_e characteristics

The two groups of cyclones, high-θ_e and low-θ_e, display clear differences in their mean θ_e, temperature and humidity. As the groups were defined based on their θ_e at 1000-850 hPa (see Section 3.3), this difference is naturally largest close to the surface, where the mean θ_e is in the range of 255-265 K for the low-θ_e group (blue), and in the range of 280-290 K for the high-θ_e group (Figure 3.1). The difference at the surface between the two groups is therefore 15-35 K. Further up in the atmosphere, the two groups are less clearly separated, with more similar θ_e values and larger variations within each group. As θ_e is a function of temperature and specific humidity, we want to study the variability of these variables as well. Both temperature and humidity show similar patterns as θ_e, with lower values seen in the low-θ_e group and higher values seen in the high-θ_e group, with the largest difference at the surface and decreasing difference with height.

The cyclones in the high-θ_e and low-θ_e groups differ in their locations of genesis and paths. Figure 4.1 shows the genesis location of each cyclone (dots) and the cyclone tracks (lines). Although there is quite a large spread in genesis location, the two groups cluster at different locations, hinting that the sources of baroclinicity and hence foundation for cyclogenesis may be different for the two groups. The cyclones in the low-θ_e group (blue) seem to cluster mostly along the sea ice edge, suggesting that these cyclones are created from baroclinicity due to the ocean-sea ice interface. In contrast, the cyclones in the high-θ_e group (red) cluster mostly to the southeast of Greenland and in the North Atlantic. This suggests that these cyclones are created from orographic processes or as secondary genesis from cyclones originating further south in the North Atlantic. These suggestions will be further explored in Chapter 5: *Discussion*. In addition, the two groups exhibit different pathways. The cyclones in the high-θ_e group tend to move northeast from genesis, while most of the cyclones in the low-θ_e group tend to move east/southeast from genesis.

4.2 Isentropic overturning of low-θ_e and high-θ_e cyclones
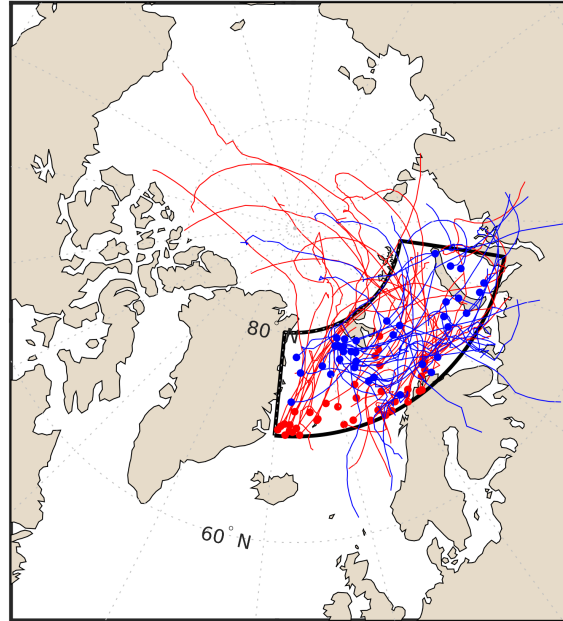
Figure 4.1: Cyclone tracks for the high-θ_e (red) and low-θ_e (blue) groups. The dots mark the genesis location, while the lines show the cyclone paths over the whole course of their lives. The black contour shows the study region.

4.2.1 Isentropic mass flux

The isentropic mass flux shows the isentropic overturning of air parcels for the two cyclone group composites. As described in Section 3.4, the mass flux is calculated using an isentropic analysis framework. Figure 4.2 shows the mass flux evolution from 6 hours after genesis to 48 hours after genesis for the high-θ_e (4.2a) and low-θ_e (4.2b) groups. The isentropic mass flux is shown as a function of θ_e and height, displayed in pressure levels. Cyclones in both groups display a clear thermally direct circulation, with higher θ_e air rising (positive mass flux, red colours) and lower θ_e air sinking (negative mass flux, blue colours).

Comparing the mass flux for the two groups, we see several differences in the isentropic overturning. The mass flux for the high-θ_e group reaches a height of 400 hPa, while most of the mass flux for the low-θ_e group is confined to below 500-600 hPa, demonstrating that the cyclones in the high-θ_e group have deeper overturning circulation compared to the cyclones in the low-θ_e group. A deeper circulation for the high-θ_e cyclones implies that the air parcels in the high-θ_e cyclones will need to travel farther up in the atmosphere before they become denser than the surroundings and start descending, compared to air parcels in the low-θ_e cyclones. This may be explained by assuming that the environmental lapse rate is equal for both groups and that they both follow the moist adiabatic lapse rate, which is around 6 K/km. Based on these assumptions, the warmer and moister air parcels at the surface belonging to the high-θ_e cyclones would have to travel a longer vertical distance to reach the surrounding environmental temperature. In addition, although the low-θ_e group is confined to a lower level of the troposphere (1000-600 hPa), the low-θ_e mass flux is stronger than the high-θ_e mass flux at these pressure levels, indicating a higher rate of mass transport over

time. After 48 hours, the high-θ_e group exhibits nearly no mass flux, while the low-θ_e group still shows a clear thermally direct circulation. The cyclones in the high-θ_e group therefore decay more rapidly compared to the cyclones in the low-θ_e group.
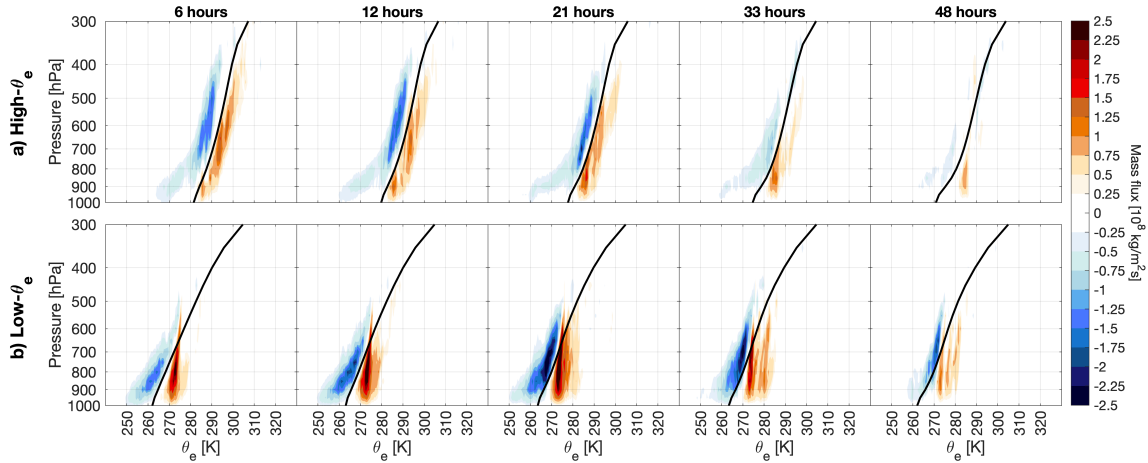

Figure 4.2: The evolution of the isentropic mass flux $[kg/m^2s]$ for the a) high-θ_e and b) low-θ_e groups from 6 hours after genesis to 48 hours after genesis. Positive mass flux (red) shows ascending air parcels, while negative mass flux (blue) shows descending air parcels. Stronger mass flux indicates a higher rate of mass transport over time. The black line shows the vertical profile of mean θ_e.

The vertical profile of the mean θ_e shows a difference in both its magnitude and evolution between the two groups. The black line in Figure 4.2 represents the mean θ_e for each group at each pressure level. At 6 hours after genesis, the high-θ_e composite has a mean θ_e of 282 K at the surface, while the low-θ_e composite has a mean θ_e of 262 K. At the 300 hPa pressure level, the high-θ_e composite has a mean θ_e of 307 K while the low-θ_e composite has a mean θ_e of 305 K. This means that the cyclones in the low-θ_e group have a much larger difference in θ_e between the surface and the top of the troposphere and thus a steeper θ_e gradient with height compared to the cyclones in the high-θ_e group. However, as the overturning circulation is shallower for the low-θ_e cyclones than for the high-θ_e cyclones, the θ_e difference between the surface and top of circulation is nearly the same for the two groups, with a θ_e difference of just above 20 K. The difference in mean θ_e between the two groups decreases over time, as the low-θ_e cyclones increase slightly in mean θ_e, while the high-θ_e cyclones decrease in mean θ_e. However, the evolution of mean θ_e varies with pressure level, with larger changes close to the surface than farther up in the troposphere (Figure B.1). At surface level (1000 hPa), there is a clear difference in mean θ_e between the two groups at 6 hours after genesis that decreases over time. Interestingly, at around 65 hours after genesis, the high-θ_e composite has a lower mean θ_e than the low-θ_e composite, albeit a small difference. In the middle of the troposphere (700 hPa), the two groups still differ markedly, but near the top of the troposphere (300 hPa) the two groups have approximately the same mean θ_e.

The tilt of the ascending or descending mass flux likely demonstrates the effect of

air parcels mixing with the surrounding environment. Air parcels crossing the isentropic surfaces indicate a presence of entrainment (mixing of environmental air into the convective air parcels) or detrainment (mixing of convective air parcels into the environment), where the air parcels undergo a change in heat and/or moisture (chapter 14 in *Hoskins and James*, 2014). A larger tilt of the ascending or descending mass flux therefore indicates that the cyclones and the surrounding environment exchange a larger amount of heat or moisture. For the low-θ_e group, the ascending motion is nearly vertical while the descending motion is tilted, signifying that the ascending motion is characterised by nearly moist-adiabatic movement, while the descending motion experiences entrainment. Therefore, the rising air parcels undergo little to no mixing with the environment, while the sinking air parcels likely mix with the environment as they subside. When the air parcels mix with the lower θ_e air in the surrounding environment, the θ_e of the subsiding air parcels decreases. The lower half (pressure levels 1000-700 hPa) of the mass flux belonging to the high-θ_e group displays similar characteristics, with a stronger tilt in the descending mass flux compared to the ascending mass flux.

4.2.2   Quantifying the difference in mass flux

The visual difference in the overturning circulation height between the high-θ_e and low-θ_e groups can be quantified by decomposing the mass flux. We decompose the mass flux into the amount of mass flux below and above 700 hPa at 6 hours after genesis and 33 hours after genesis (Figure 4.3). Each dot shows the distribution of an individual cyclone in the high-θ_e (red) or low-θ_e (blue) group, and the *x* marks the distribution of the two group composites. As the cyclones exhibit large variability in the amount of mass flux, a linear regression is fitted to each group to better identify the difference between the two groups. The linear regression line is based on the total least squares method (*Markovsky and Van Huffel*, 2007), minimising the error in the mass flux both below and above the 700 hPa level. We want to minimise the error both above and below this level, as both are estimated from the total mass flux and will therefore contain some uncertainty. A line with a 1:1 relation means that there is an equal amount of mass flux above and below 700 hPa.

The circulation height differs greatly between the two groups at the start of the life cycle, but this distinction decreases as the two groups converge towards each other. At 6 hours after genesis (Figure 4.3a), we see a clear clustering of the two groups. The cyclones in the high-θ_e group have almost equal amount of mass flux above and below 700 hPa, while the cyclones in the low-θ_e group have much more mass flux below than above this level. The two composite values have the same amount of mass flux below 700 hPa, but above 700 hPa the high-θ_e composite has around $0.5 * 10^8 kg/m^2 s$ more mass flux than the low-θ_e composite. At 33 hours after genesis (Figure 4.3b), the two groups are less distinct from each other. Here, the composite values are similar in the amount of mass flux above 700 hPa, but the low-θ_e composite has around $0.5 * 10^8 kg/m^2 s$ more mass flux below 700 hPa than the high-θ_e composite. The slope of the linear regression line for the high-θ_e group has decreased from 6 hours after genesis, suggesting less mass flux above 700 hPa than below 700 hPa. Conversely, the

slope of the linear regression line for the low-θ_e group has increased from 6 hours after genesis. The two groups are therefore more similar in mass flux distribution at 33 hours after genesis than at the start of the life cycle.
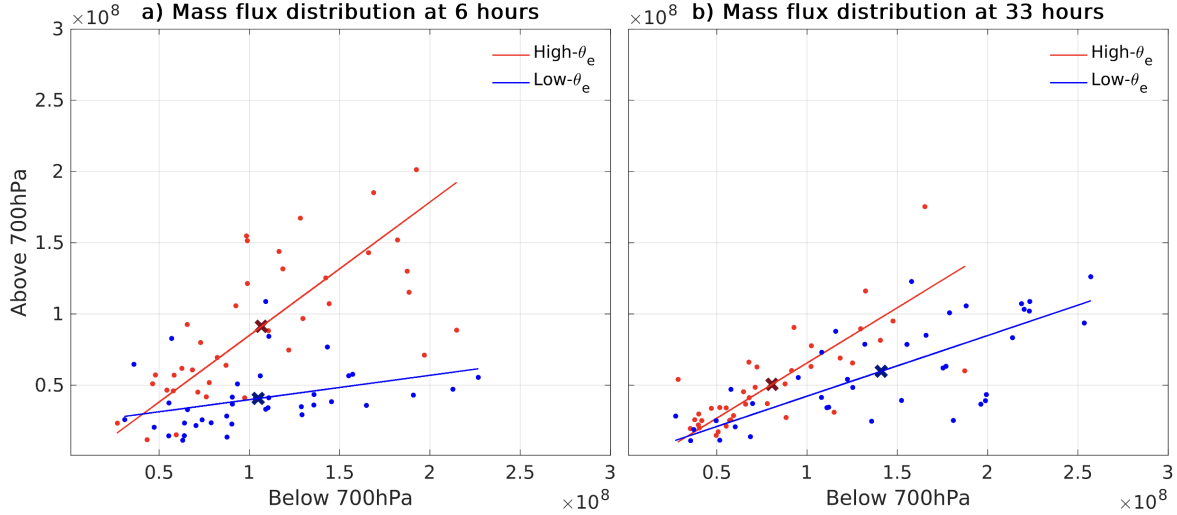

Figure 4.3: Mass flux decomposition of the high-θ_e (red) and low-θ_e (blue) groups at a) 6 hours and b) 33 hours after genesis. The mass flux $[kg/m^2 s]$ is split into total mass flux below and above 700 hPa, where each dot represents one individual cyclone. The x marks the composite value for each group, and a linear regression line is fitted to each group, using a total least squares method.

4.2.3   Vertical velocity

The vertical velocity shows differences between the high-θ_e and low-θ_e groups that point to differences in how vigorous the isentropic overturning is for the two groups. As a stronger mass flux indicates a higher rate of mass transport over time, the strength in mass flux represents the vertical velocity speed, given the similar density. Figure 4.4 shows the distribution of vertical velocity for the high-θ_e (4.4a) and low-θ_e (4.4b) groups from 6 hours after genesis to 48 hours after genesis. The shading indicates the total area of a specific vertical velocity at a given pressure level, based on the area enclosed within a 500 km radius around the cyclone centre. Both groups show a large area of near-zero vertical velocities at the surface (red colours), as expected due to the rigid surface boundary and the weak horizontal velocities due to friction. The red colours at near-zero vertical velocities are also seen near the top of the troposphere for the low-θ_e group, illustrating the limited circulation at the upper pressure levels for the low-θ_e cyclones. This concurs with the mass flux (Figure 4.2), where the cyclones in the low-θ_e group have shallower circulation than the high-θ_e group.

Comparing the shapes in the vertical velocity distribution shows that the highest velocities can be found at different pressure levels in the troposphere for the two groups and that the magnitude of the updrafts and downdrafts differ in both groups. The low-θ_e group shows a bottom-heavy shape (seen by the outline of the weaker blue colours), with areas of strong updrafts and downdrafts at pressure levels 900-700 hPa, compared

to the large area of weaker updrafts and downdrafts further up in the troposphere. On the other hand, the high-θ_e group shows a more symmetric shape with higher vertical velocities around 600-400 hPa. This indicates that the cyclones in the low-θ_e group have more vigorous overturning circulation closer to the surface, while the cyclones in the high-θ_e group have more vigorous circulation further up in the troposphere. Additionally, there is a skewness between the positive and negative vertical velocities seen in both groups, with larger areas of strong updrafts than strong downdrafts. This asymmetry demonstrates that the air parcels ascend more rapidly up in the troposphere, and descend more slowly back to the surface.
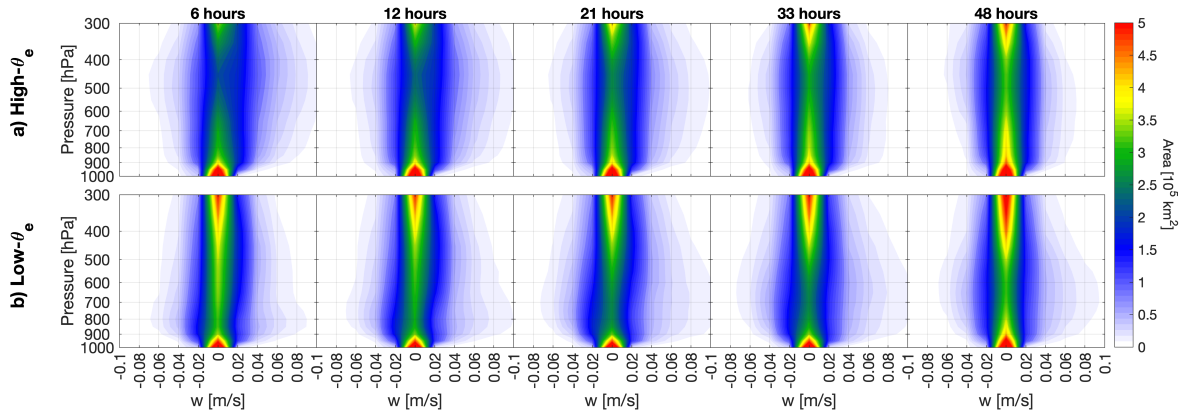

Figure 4.4: Evolution of the vertical velocity distribution [m/s] for the a) high-θ_e and b) low-θ_e groups from 6 hours after genesis to 48 hours after genesis. The shading indicates the area of a specific vertical velocity at a given pressure level, based on the area enclosed within a 500 km radius around the cyclone centre.

4.2.4 Isentropic streamfunction

The overturning circulation can be visualised by the isentropic streamfunction that illustrates the mean trajectories of the air parcels. As discussed in Section 3.4, the streamfunction is calculated by integrating the mass flux over all θ_e values. Figure 4.5 shows the streamfunction evolution for the high-θ_e (4.5a) and low-θ_e (4.5b) groups from 6 hours after genesis to 48 hours after genesis. At locations where ≤ 2 cyclones in the group exhibited a streamfunction value, pale grey crosses are added, indicating that the streamfunction should be disregarded. This is mostly on the upper left side of the streamfunction, i.e., where the air parcels descend. The negative streamfunction indicates a counterclockwise movement of the air parcels along the streamlines (lines of constant streamfunction magnitude), thus displaying a thermally direct circulation, consistent with the mass flux. The horizontal streamlines close to the surface are likely due to surface fluxes, where heat is exchanged from ocean to atmosphere, increasing the θ_e of the air parcels closest to the surface. Similar to the tilt in the updrafts and downdrafts in the mass flux, the slope of the streamline illustrates the entrainment rate of the air parcels (*Pauluis and Mrowiec*, 2013), where near-vertical streamlines indicate almost no entrainment and near-horizontal streamlines indicate strong entrainment. Both group composites display tilted streamlines and thus strong entrainment on the left-hand side of the streamfunction, indicating mixing of the descending air parcels

with the environment. The ascending air parcels, however, undergo little entrainment, shown by the near-vertical streamlines in both groups.

The streamfunction shows different overturning circulation depth and width between the two groups, in agreement with the findings from the mass flux and vertical velocity. The circulation depth between the two groups clearly differs, where the streamfunction belonging to the high-θ_e group reaches higher heights than the streamfunction belonging to the low-θ_e group, indicating deeper circulation for the former than the latter. Additionally, the circulation width differs between the two groups. The width of the high-θ_e streamfunction is nearly 30 K close to the surface (1000-900 hPa), but farther up in the troposphere the streamfunction extends in a narrower arm with a width of 15-20 K. The low-θ_e streamfunction has a similar, but slightly larger, width close to the surface of around 30 K, but lacks this narrow area at higher heights. Although the cyclones in the low-θ_e group have shallower circulation, the centre of circulation displays a stronger negative streamfunction, indicating a higher rate of air mass transport compared to the centre of circulation in the cyclones belonging to the high-θ_e group.
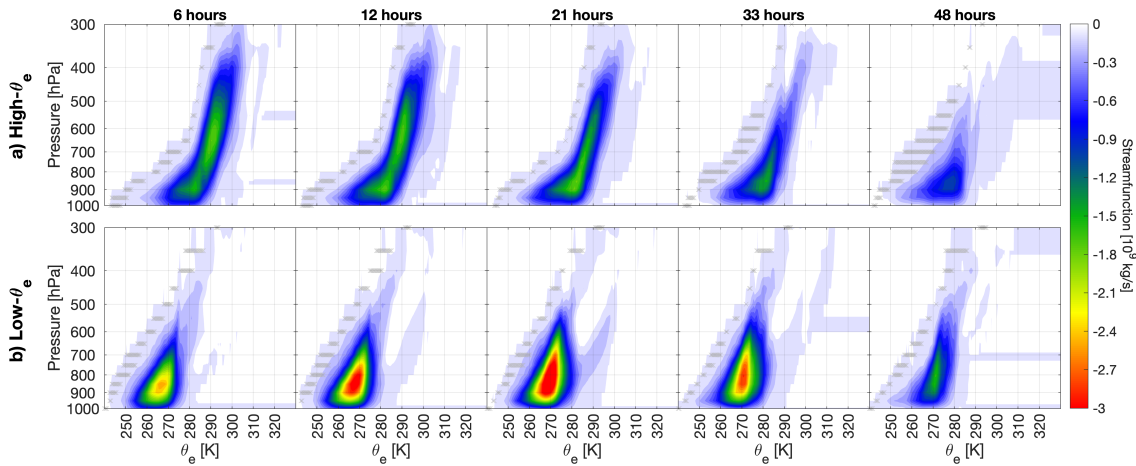
Figure 4.5: Evolution of the isentropic streamfunction [kg/s] for the a) high-θ_e and b) low-θ_e groups from 6 hours after genesis to 48 hours after genesis. Decreasing values towards the circulation centre indicate a counterclockwise movement of the mean air parcel trajectory, following lines of constant streamfunction magnitude (streamlines). Pale grey crosses indicate locations where ≤ 2 cyclones in the group exhibit a streamfunction value, and should therefore be disregarded.

The evolution of the streamfunction from 6 hours to 48 hours after genesis shows differences in the circulation strength and shape that relate to how the cyclones in the two groups develop. The high-θ_e composite has both its deepest and strongest circulation at 6 hours, followed by a weakening in strength and decreasing circulation depth over time. The height of the overturning circulation changes from 350 hPa at 6 hours after genesis to 650 hPa at 48 hours after genesis. On the other hand, the low-θ_e composite has similar circulation height throughout the period, and strengthens up to 21 hours after genesis, when the circulation is at its maximum strength, before weakening. In addition, the streamfunction is strongest at different θ_e values between the two groups,

where the maximum streamfunction strength for the high-θ_e composite (at 290 K) is located at a θ_e that is 25 K higher than the maximum streamfunction strength for the low-θ_e composite (at 265 K). This difference decreases over time, as the low-θ_e streamfunction evolves towards slightly warmer θ_e air and the high-θ_e streamfunction evolves towards colder θ_e air, indicating that they both converge towards some climatological θ_e level. At 48 hours, the two group composites display similar streamfunctions.

4.2.5 Uncertainty estimates on the streamfunction

Despite the small sample sizes, we find that the streamfunction group composites represent reasonably well the circulation of any given cyclone. As there is large variability in streamfunction strength between the individual cyclones, simple significance tests will most likely not show any significant results. Further, a simple probability density function assumes a normal distribution of the data, which we cannot assume due to the small sample size. Instead, we use a kernel density estimate, which is one type of a probability density estimate, as it estimates the probability of a variable at specific grid cells without the need to assume a normal distribution (*Chen*, 2017). We only include streamfunction values stronger than $-5*10^9 kg/s$ for each individual cyclone. Note that the kernel density estimate gives the probability of the streamfunction in (θ_e,P) space but does not say anything about the streamfunction magnitude. Darker red colours in Figure 4.6 indicate a higher frequency of individual cyclone streamfunctions at a specific location in (θ_e,P) space. The white line shows the contour of $-1*10^9 kg/s$ from the streamfunction group composites, to more easily compare the locations of the composites and distributions in (θ_e,P) space. Although there is a large spread between the individual cyclones, the distribution from the kernel density estimate has its highest frequencies coinciding with the streamfunction composite. This means that the shape of the streamfunction composites represents most of the individual cyclones for both groups and at each time step.

The distribution of streamfunction within each group varies over time. The highest probability of occurrence for the high-θ_e group is around 285 K and 900-850 hPa at 6 hours after genesis. Over time, the location of the highest probabilities becomes more concentrated in (θ_e,P) space and shifts colder/drier as well as upward to 270-280 K and 900-800 hPa at 48 hours after genesis. The increase in concentration of the distribution indicates that the cyclones in the high-θ_e group have a larger spread at 6 hours after genesis, but converge towards a more similar circulation at 2 days after genesis. The highest probability of occurrence for the low-θ_e group is at 260-270 K and 950-800 hPa at 6 hours after genesis. Over time, the location of the highest probabilities becomes more dispersed in (θ_e,P) space, and the highest density shifts slightly warmer/moister as well as upward to around 270 K and 900-800 hPa. The increased dispersion of the distribution means that most of the cyclones in the low-θ_e group have similar circulations at 6 hours after genesis, but have a large spread in circulation after 2 days.

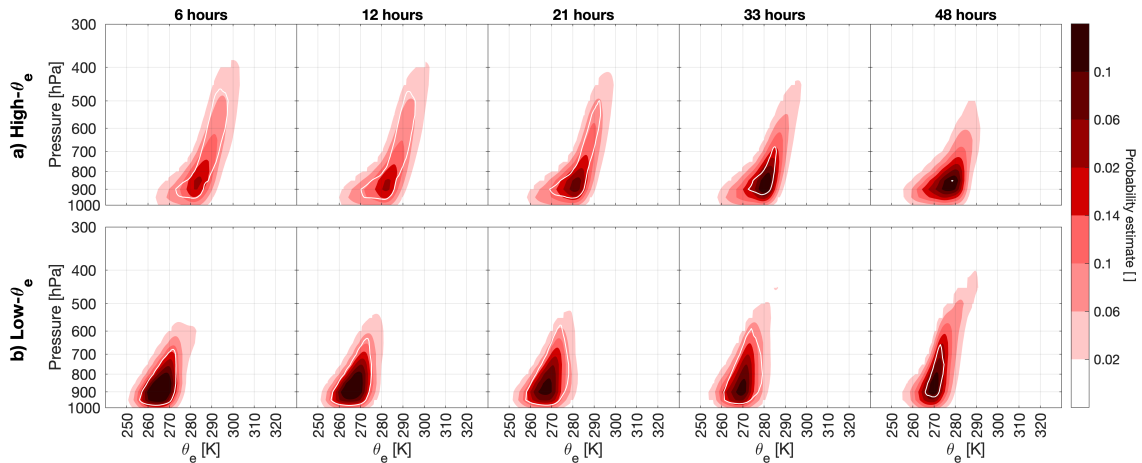*Figure 4.6: Evolution of the distribution of streamfunction $[kg/s]$ in each group based on a probability estimate for the a) high-θ_e and b) low-θ_e groups from 6 hours after genesis to 48 hours after genesis. Higher values indicate a higher probability of occurrence of the streamfunction within each group. The white contour shows the contour of the streamfunction composite at $-1 * 10^9 kg/s$.*

4.2.6   Summary of the overturning circulation

Studying the mass flux, vertical velocity and streamfunction together, we can get a good summary of the overturning circulation for the two groups. Figures 4.2-4.6 all show that the cyclones in the high-θ_e group have deeper overturning circulation than the cyclones in the low-θ_e group, with a wider base close to the surface and a narrower arm stretching further up in the troposphere to around 350 hPa. Further, the cyclones in the low-θ_e group have overturning circulation confined to below 500-600 hPa, and an overall wider base than the cyclones in the high-θ_e group. Although the low-θ_e cyclones have shallower overturning circulation, the circulation is more vigorous at the lowermost 300 hPa (Figure 4.4), resulting in a stronger mass flux and streamfunction for the low-θ_e cyclones than the high-θ_e cyclones. Further, the high-θ_e cyclones have a higher mean θ_e throughout most of the troposphere, while the low-θ_e cyclones have a steeper gradient in mean θ_e with height (Figure 4.2). While there is large variability within each group, the kernel density estimate shows that the group composites still represent the individual cyclones reasonably well (Figure 4.6). Additionally, the streamlines corresponding to the descending air parcels have a stronger tilt than the streamlines corresponding to the ascending air parcels (Figure 4.5). This tilt represents air parcels crossing the isentropes (lines of constant θ_e) and indicates diabatic effects, i.e., that there is a transfer of heat and/or moisture between the sinking air parcels and the environment. For example, surface fluxes can affect both temperature and moisture of the air parcels close to the surface, and entrainment further up in the troposphere can decrease the mean θ_e. Also, the vertical velocity shows that the ascending air has in general stronger vertical velocities than the descending air. Therefore, the ascending air has a more rapid and near-adiabatic motion while the descending air has a slower and more diabatic motion.

4.3   Evolution of cyclone strength and energy

The previous section shows that the isentropic overturning differs between the two groups, and thus we want to further compare the evolution of the strength and energy release related to these groups. The strength and energy release can indicate how much the cyclones affect the surrounding environment and when they are at their most intense. In addition, we want to explore if and in what way the strength and energy release are markedly different. As both groups exhibit large variability, we use an uncertainty estimate to check if the group medians are meaningful.

4.3.1   Strength and energy of isentropic overturning

The sea level pressure (SLP) shows differences in strength evolution between the two groups. Figure 4.7 shows the evolution of SLP for both groups, both in absolute SLP (4.7a) and as the anomaly from the first time step value for the high-θ_e (4.7b) and low-θ_e (4.7c) groups, presenting the evolution relative to genesis. The thin lines represent the individual cyclones, while the thick lines represent the group medians. Although there is large variability within both groups, indicating that the difference between the group medians may be insignificant by standard measures, visually the medians show clear differences that might still be meaningful. The cyclones in the high-θ_e group have lower SLP than the cyclones in the low-θ_e group throughout the life cycle, with the largest difference of 25 hPa observed at genesis. This shows that the high-θ_e cyclones are in general stronger than the low-θ_e cyclones. Further, the evolution differs between the two groups, as the low-θ_e cyclones strengthen for the first 24 hours before weakening, while the high-θ_e cyclones are at their lowest pressures for the first 24 hours. This is more clearly seen when studying the evolution as anomaly from genesis, where the SLP belonging to the high-θ_e cyclones lowers slightly before increasing, while the SLP belonging to the low-θ_e cyclones lowers more and over a longer time period, before returning to the same pressure as the genesis pressure. The difference in SLP between the two groups concurs with the evolution of cyclone depth, where the high-θ_e cyclones generally have a greater depth than the low-θ_e cyclones (Figure B.2). This is expected as the cyclone depth is given as the difference between the centre of the low-pressure and the surrounding pressure, and thus is correlated with the SLP. While the depth of the high-θ_e group median varies between 8-10 hPa over the time period, the low-θ_e group median has an average depth of around 4 hPa close to genesis, increasing steadily to around 8 hPa after 48 hours.

Studying the intensity of the isentropic overturning, the maximum strength of the streamfunction shows a difference in the vigour of the overturning circulation connected to each group. Figure 4.8a-c shows the evolution of the maximum streamfunction strength for the two groups, both in absolute values (4.8a) and as anomaly from the first time step for the high-θ_e (4.8b) and low-θ_e (4.8c) groups. A running mean of 6 hours has been applied to smooth the results, meaning that the first time step is at 9 hours after genesis (note that the first time step of the streamfunction is at 6 hours after genesis and the data has an interval of 3 hours between two steps). The individual cyclones are shown as thin lines while the group medians are shown as thick lines.
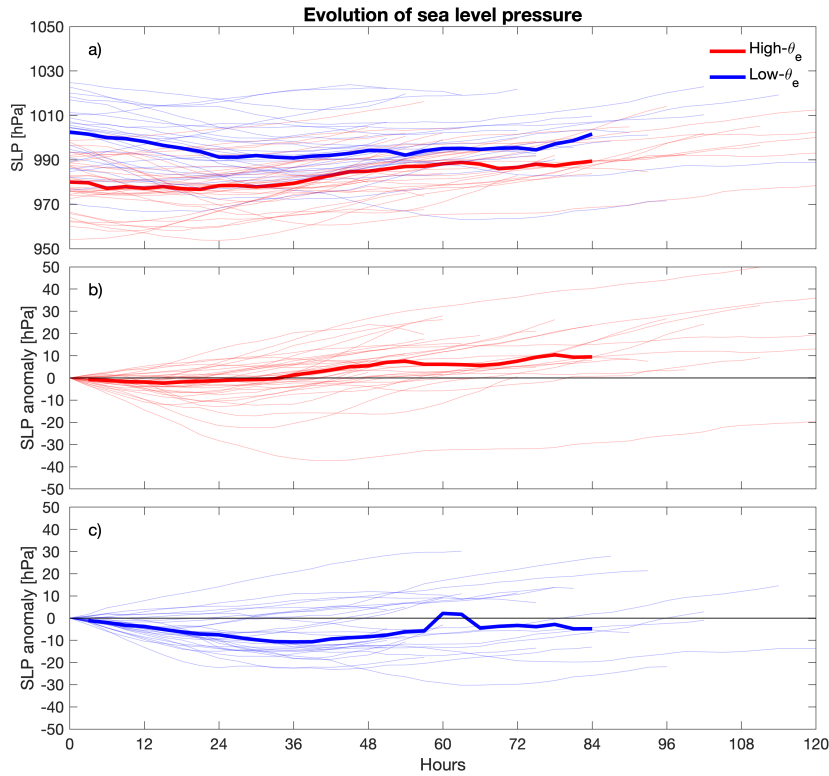
Figure 4.7: Evolution of sea level pressure (SLP) [hPa] for the high-θ_e (red) and low-θ_e (blue) groups. The evolution is shown both as a) the absolute SLP for both groups and as the anomaly from the first time step for the b) high-θ_e and c) low-θ_e groups. Thin lines show the evolution for each individual cyclone while the thick lines show the medians for each group.

Both groups exhibit a large spread in streamfunction strength, demonstrating large variability between the individual cyclones. However, the group medians display a visual difference between the two groups. While both group medians show similar maximum streamfunction strength at 9 hours after genesis, the low-θ_e median strengthens while the high-θ_e median solely weakens over time. The low-θ_e median reaches its peak strength of around $-2.5 * 10^{10} kg/s$ at 24 hours after genesis before decaying. After 3 days the maximum strength of the low-θ_e median is as weak as the high-θ_e median, signifying a more rapid decline of streamfunction strength for the low-θ_e cyclones after 24 hours. The difference in evolution between the two groups is also clear when looking at the anomaly from the first time step. While the cyclones in the low-θ_e group increase in strength, the cyclones in the high-θ_e group weaken throughout the whole life cycle.

While there are visual differences between the two groups, the large variability within each group means that the two group medians may not be significantly different from each other. We observe a clear peak in maximum streamfunction strength for the low-θ_e group, but we cannot properly assess solely from the figure whether this peak is representative for the group. To assess whether the group medians represent the individual cyclones well, an uncertainty estimate is calculated in the next section. The increase

in strength at 80 hours seen for the low-θ_e group can likely be ignored, as many of the cyclones have died out, causing the median to be based on only a few cyclones. There is also large variability within the two groups when studying the height and width of the streamfunction. Visually, the high-θ_e cyclones have their maximum streamfunction strength located at higher heights (Figure B.3), and are both deeper and narrower in the overturning circulation than the low-θ_e cyclones (Figures B.4 and B.5). The differences are largest close to genesis and decrease over time, and after 30 hours we can no longer see a clear visual difference between the two groups. While we see a visual difference for the first 30 hours, the large variability within each group compared to the difference between the medians indicates that this visual difference is likely not significant.
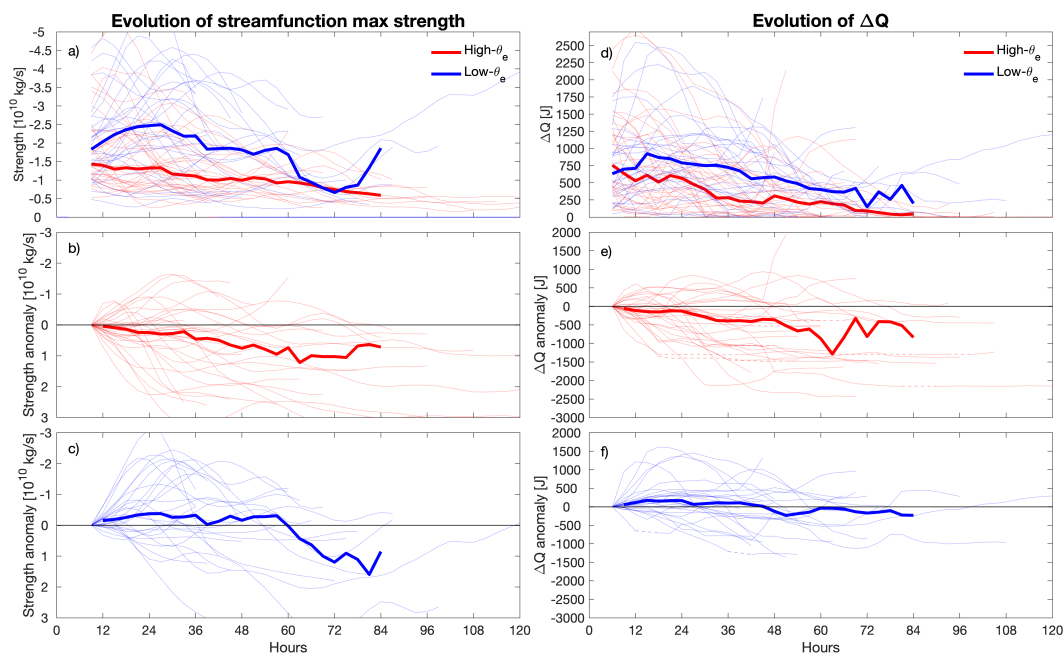

Figure 4.8: Evolution of a-c) maximum streamfunction strength $[kg/s]$ and d-f) heat release (ΔQ) $[J]$ for the high-θ_e (red) and low-θ_e (blue) groups. The evolution is shown both as a,d) the absolute value for both groups and as the anomaly from the first time step for the b,e) high-θ_e and c,f) low-θ_e groups. Thin lines show the evolution of each individual cyclone, while the thick lines show the medians for each group.

The heat released by the isentropic overturning differs between the two groups, with evolutions similar to the intensity evolutions. A more vigorous (and therefore more intense) overturning circulation means that the air parcels in the isentropic overturning move more quickly, implying a higher kinetic energy. This energy can be released in the form of heat, and we therefore want to study the heat release (ΔQ) connected to the isentropic overturning. ΔQ is calculated based on the area of the streamfunction (see Section 3.4), and Figure 4.8d shows the evolution of ΔQ. Similarly to the SLP and maximum streamfunction strength, there is large variability between the individual cyclones within each group (thin lines), but there are still some visual differences between the group medians (thick lines). Both group medians show a ΔQ of 500-750 J at

6 hours after genesis, with the high-θ_e median having a slightly larger ΔQ. Over time, the low-θ_e cyclones increase in ΔQ for the first 15 hours before decreasing, while the high-θ_e cyclones have their highest ΔQ at 6 hours after genesis and decrease over time.

To see a clearer difference in evolution between the two groups, ΔQ evolution can be shown relative to genesis. Figure 4.8e-f shows the evolution of ΔQ as the anomaly from the first time step for both the high-θ_e (4.8e) and the low-θ_e (4.8f) groups. While the high-θ_e cyclones are at their maximum at genesis and have a negative anomaly evolution, the low-θ_e cyclones have a positive anomaly evolution for the first 2 days. It is worth noting that for a few of the cyclones at specific time steps, the streamfunction had no values stronger than the threshold, resulting in no ΔQ estimate and therefore a gap in the timeseries. To make the timeseries continuous, dashed lines have been added to illustrate this gap. The evolution of the ΔQ anomalies supports the evolution of circulation intensity, shown by the maximum strength of the streamfunction. Overall, the high-θ_e cyclones have a more rapid decrease in intensity and ΔQ, while the low-θ_e cyclones have a larger time period of increasing intensity and ΔQ before decaying.

4.3.2 Uncertainty estimates on strength and heat release

Studying the distribution of SLP within each group, we find that the group medians can give a reasonable picture of SLP evolution. Similar to assessing the uncertainty of the streamfunction, we apply a kernel density estimate to study the uncertainties of the SLP anomalies (Figure 4.9). Darker red colours indicate a higher probability of specific SLP anomaly values. Although there is a widespread distribution within each group, the highest probability of occurrence in the kernel density estimate coincides with the group medians. The highest probability of occurrence is around 0 hPa for the first 12 hours for both groups, indicating small changes in SLP at the start of the life cycle. After 12 hours, the low-θ_e group shows a higher probability below 0 hPa, suggesting most of the cyclones decrease in SLP over time (Figure 4.9b). There is also a high probability above 0 hPa after 36 hours, likely because some of these cyclones have shorter life cycles and therefore weaken at earlier time steps. On the other hand, the high-θ_e group shows a higher probability above 0 hPa, suggesting most of the cyclones increase in pressure over time (Figure 4.9a).

The distributions of maximum streamfunction strength and ΔQ within each group also show that the group medians represent the evolutions of the groups well. Figure 4.10 shows the probability estimate from the kernel density estimate for maximum streamfunction strength (4.10a,b) and ΔQ (4.10c,d) anomalies. Similarly to the SLP, there is a widespread distribution within each group, but the highest probability of occurrence (darkest colours) in the kernel density estimate still coincides with the group medians. The highest probability of occurrence in maximum streamfunction strength for the high-θ_e group is around and below 0 kg/s. The low-θ_e group, however, shows the highest probability around and above 0 kg/s. This concurs with the group medians of both groups, as seen in Figure 4.8b,c. The highest probability of occurrence in ΔQ anomaly is along 0 J for both groups, suggesting most of the cyclones have small changes in ΔQ.
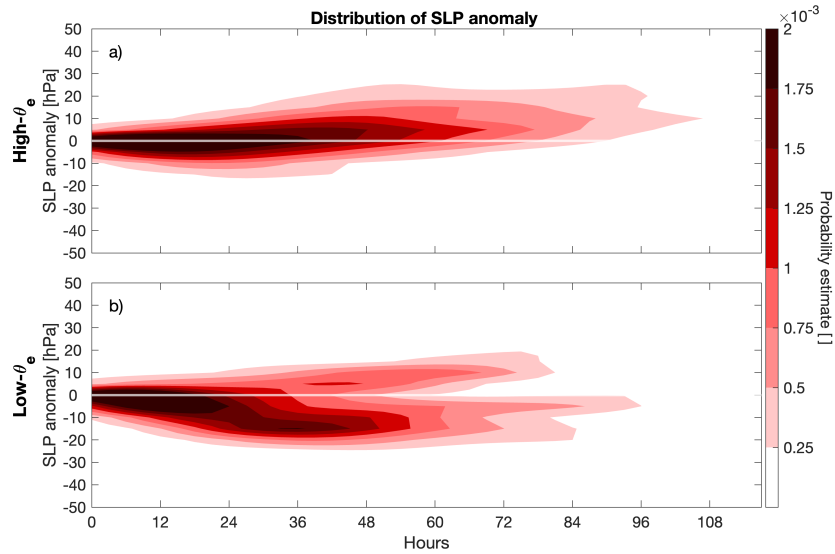
Figure 4.9: Evolution of the distribution of sea level pressure (SLP) [hPa] anomalies for the a) high-θ_e and b) low-θ_e groups. Darker colours indicate a higher probability of occurrence of the SLP anomalies within each group.

Although there are small changes in ΔQ, the high-θ_e group shows a higher probability below 0 J (4.10c), while the low-θ_e group shows a higher probability slightly above 0 J (4.10d). This concurs with the group medians of the ΔQ anomaly evolutions seen in Figure 4.8e,f.
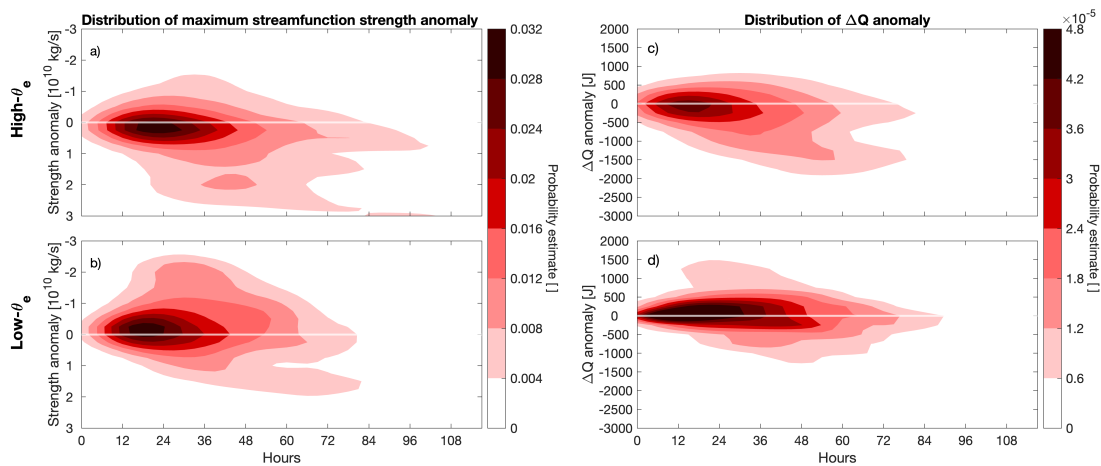
Figure 4.10: Evolution of the distribution of a,b) maximum streamfunction strength [kg/s] and c,d) heat release (ΔQ) [J] anomalies for the a,c) high-θ_e and b,d) low-θ_e groups. Darker colours indicate a higher probability of occurrence of maximum streamfunction strength anomalies or heat release anomalies within each group.

4.3.3 Comparison of high-θ_e and low-θ_e evolutions

While there is large variability within the high-θ_e and low-θ_e groups, the two groups exhibit different evolutions related to both strength and energy. The high-θ_e group shows

a lower SLP median of around 25 hPa compared to the median belonging to the low-θ_e group at genesis (Figure 4.7). However, the evolution of the maximum streamfunction strength shows that the cyclones in the low-θ_e group have a larger maximum strength and therefore a more vigorous overturning circulation than the cyclones in the high-θ_e group (Figure 4.8a-c), supporting the findings from Section 4.2. The larger maximum strength relates to the higher ΔQ seen in the low-θ_e group compared to the high-θ_e group during most of the life cycle (Figure 4.8d-f). Although there is a clear visual difference between the two groups, which we believe might be meaningful, these differences might be insignificant using standard significance tests because of the large variability within each group and the small sample size. For example, the peak in intensity and strength seen in the low-θ_e group will not necessarily be significant using a standard significance test. Nevertheless, we checked the representativeness of the group medians using a kernel density estimate. While there is a large distribution in SLP, maximum streamfunction strength and ΔQ anomalies within all groups, the kernel density estimates support the findings from the group medians of the anomaly evolutions, with most of the cyclones strengthening at the start of the life cycle in the low-θ_e group and most of the cyclones weakening in the high-θ_e group.

4.4 Difference in Arctic environment and cyclone impact

Cyclones are important for the local climate as they influence the atmosphere and ocean along their paths. We therefore want to study the Arctic environment for the high-θ_e and low-θ_e groups to assess the differences in the impact between these groups. This can indicate what climate the cyclones are related to, as well as how the two groups affect different parts of the atmosphere and surface, such as the surface energy budget and precipitation type and strength. Unless specified otherwise, the maps show the group composite of the Arctic environment based on genesis day for each cyclone. The daily anomalies are anomalies with respect to monthly-mean climatology when removing the long-term trend, to see the cyclone impacts independent of Arctic warming during the study period.

The spatial signatures of the temperature and specific humidity show opposite anomaly patterns for the two groups. Figure 4.11 shows the 2m temperature and specific humidity anomalies for the low-θ_e (4.11a and 4.11c, respectively) and high-θ_e (4.11b and 4.11d, respectively) groups. The high-θ_e (low-θ_e) group displays a warmer (colder) than normal surface atmosphere in the study area, where the low-θ_e group has its strongest anomaly just east of Svalbard and the high-θ_e group has its strongest anomaly at the northernmost part of the Nordic countries. Similarly, the maps show a more (less) humid atmosphere in the study region for the high-θ_e (low-θ_e) group. A warmer and moister atmosphere for the high-θ_e cyclones and a colder and drier atmosphere for the low-θ_e cyclones are expected, based on the vertical profiles of mean temperature and humidity seen in Figure 3.1. Additionally, there is a large-scale tripole pattern seen on the temperature maps, with positive (negative) anomalies in the study region and negative (positive) anomalies both west/southwest of the study region and northeast of the study region for the high-θ_e (low-θ_e) group. The humidity maps show a similar pattern except for the anomaly northeast of the region, thus displaying a dipole pattern

between the study region and southwest of region. The findings from the temperature and humidity maps agree with the maps of θ_e anomalies that show the same patterns, as expected (Figure C.1).
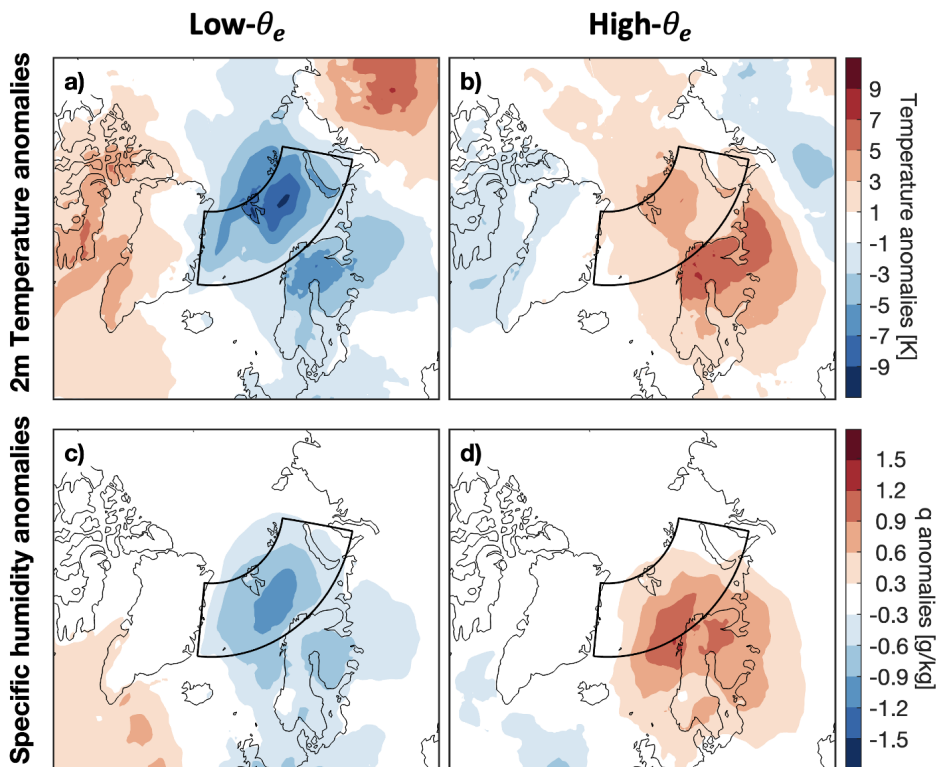

Figure 4.11: Maps of the a,b) 2m temperature $[K]$ and c,d) specific humidity (q) $[g/kg]$ anomalies for the a,c) low-θ_e and b,d) high-θ_e groups. The black contour shows the study region. Red colours indicate warmer (moister) than climatology while blue colours indicate colder (drier) than climatology for the temperature (humidity) maps.

The temperature and humidity evolutions show anomalous values several days before genesis, suggesting the groups are related to a preconditioned environment. Figure 4.12 shows the daily evolution of mean temperature (4.12a) and humidity (4.12b) anomalies from 4 days before genesis to 4 days after genesis. The histograms show probability distributions estimated by a bootstrap resampling analysis, which is a statistical method that uses random sampling to obtain a distribution, and is well suited for cases with small sampling sizes (*Mooney and Duval*, 1993). The bootstrap distribution has been estimated by drawing 38 random cyclones (with replacement) each time over 2000 iterations, based on all 378 cyclones originating in the study region. The two groups show significant differences based on the bootstrap distribution, with warmer and moister anomalies for the high-θ_e cyclones (red) and colder and drier anomalies for the low-θ_e cyclones (blue). The strongest anomalies are at genesis day (day 0) for both groups and both variables. In addition, the low-θ_e group displays nearly as strong anomalous temperature and humidity 1 day before genesis (day -1), suggesting a preconditioning of a cold and dry atmosphere before cyclogenesis. The high-θ_e group also displays anomalous temperature and humidity several days before genesis, suggesting a preconditioning of a warm and moist atmosphere, but these anomalies are not as strong as the

anomalies of the low-θ_e group. Comparing this with daily evolution maps (Figures C.2 and C.3), we see a similar preconditioned warm and humid (cold and dry) environment for the high-θ_e (low-θ_e) cyclones. The anomalies of the low-θ_e group appear to persist for some days, implying that the low-θ_e group has a longer-lasting effect on the environment after genesis compared to the high-θ_e group.
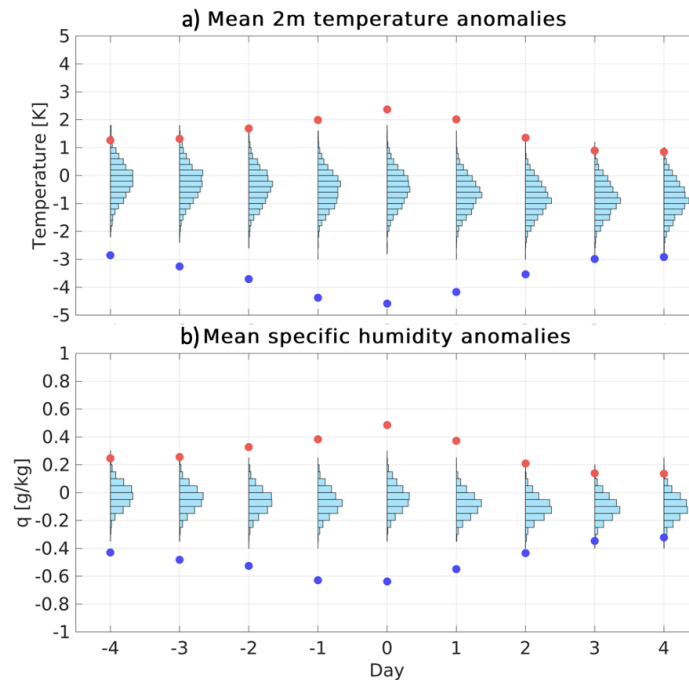

Figure 4.12: Daily evolution of a) 2m temperature $[K]$ and b) specific humidity (q) $[g/kg]$ anomalies from 4 days before genesis to 4 days after genesis, where day 0 is genesis. Histograms show the probability distribution estimated by performing a bootstrap resampling analysis. The high-θ_e (red) and low-θ_e (blue) anomalies are shown with dots for each day.

4.4.1 Surface energy budget

The surface energy budget provides insight into the impacts of cyclones on the Arctic region, as it describes the interactions between atmosphere and land/ocean. These interactions can be affected by, for example, temperature, humidity, clouds and wind. One way of studying the impacts of the high-θ_e and low-θ_e groups is therefore to study the different components of the surface energy budget. As we can neglect incoming solar radiation during the DJF winter, the relevant components of this budget when studying cyclones are the turbulent heat fluxes and the downwelling longwave radiation (DLR).

The high-θ_e and low-θ_e groups show opposite spatial patterns for the turbulent heat flux anomalies. The turbulent heat flux represents the energy exchange between ocean and atmosphere and is negative during the climatological winter, meaning that energy is exchanged from the ocean to the atmosphere. Figure 4.13a,b shows maps of the turbulent heat flux anomalies for the low-θ_e (4.13a) and high-θ_e (4.13b) groups. Positive anomalies indicate weaker heat fluxes from the ocean to the atmosphere than clima-

tology, while negative anomalies indicate stronger heat fluxes from the ocean to the atmosphere. Similarly to the temperature and humidity maps, we can clearly see a dipole structure, with negative (positive) anomalies in the study region and positive (negative) anomalies southwest of the study region for the low-θ_e (high-θ_e) group. The high-θ_e group shows a peak of 70-90 W/m^2 weaker heat flux than climatology while the low-θ_e group shows a peak of more than 90 W/m^2 stronger heat flux than climatology. While both groups show a strong anomaly in the Barents Sea entrance, the low-θ_e group also shows strong anomalies along the sea ice edge west of Svalbard. The turbulent heat flux anomalies are the sum of the sensible heat flux and latent heat flux, which display the same positive and negative dipole structure between the study region and southwest of the region (Figure C.4). Interestingly, the turbulent heat flux maps show a strong anomaly east of Greenland with an opposite sign compared to the rest of the study region, which is not seen on the temperature and humidity maps, with a strong positive (negative) anomaly for the low-θ_e (high-θ_e) group.
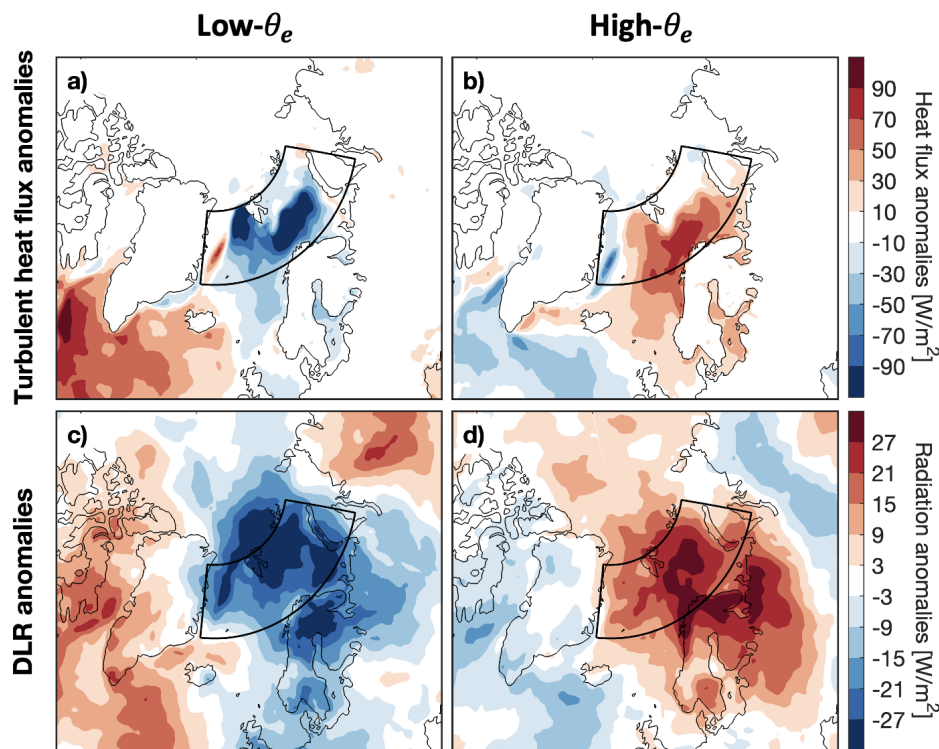

Figure 4.13: Maps of the a,b) turbulent heat flux $[W/m^2]$ and c,d) downwelling longwave radiation (DLR) $[W/m^2]$ anomalies for the a,c) low-θ_e and b,d) high-θ_e groups. The black contour shows the study region. a,b) Red (blue) colours indicate less (more) heat flux from the ocean to the atmosphere with respect to climatology. c,d) Red (blue) colours indicate more (less) longwave radiation reaching the surface with respect to climatology.

Comparing the sensible and latent heat flux anomaly maps (Figure C.4) with the air temperature and moisture anomaly maps (Figure 4.11), we see a clear connection between these variables. This connection is expected, as the sensible heat flux is a function of the temperature difference across the atmosphere-ocean interface, while the latent heat flux is a function of near-surface humidity. One region where the spatial signatures do not line up is just east of Greenland. Here, there is a negative (positive)

anomaly in the heat fluxes for the high-θ_e (low-θ_e) group that is not seen in the temperature and moisture maps, suggesting that this anomaly may be caused by other factors affecting the turbulent heat fluxes. As this anomaly is located at the sea ice edge, and sea ice hinders most of the heat transfer between ocean and atmosphere, one suggestion is that the observed anomaly is related to changes in the sea ice cover. There is likely a larger sea ice extent when cyclones in the low-θ_e group are present that will reduce the energy exchange between the ocean and atmosphere (positive anomaly), while smaller sea ice extent when cyclones in the high-θ_e group are present will allow for an increase in the energy exchange between ocean and atmosphere (negative anomaly). This can be compared with the changes in sea ice concentration, which will be discussed in the next subsection.

Another component of the surface energy budget is the DLR, exhibiting opposite anomaly patterns between the high-θ_e and low-θ_e groups, similar to previous anomaly maps. The DLR represents the amount of longwave radiation that is reflected back to the surface, for example from clouds and water droplets in the air. Figure 4.13c,d shows maps of the DLR anomalies belonging to the high-θ_e (4.13c) and low-θ_e (4.13d) groups. Here, we see a tripole structure with a positive (negative) anomaly in the study region and a negative (positive) anomaly both west/southwest and northeast of the region for the high-θ_e (low-θ_e) group. The strongest anomaly for the low-θ_e group is located over Svalbard and along the sea ice edge, while the strongest anomaly for the high-θ_e group is located over the Barents Sea entrance. As the DLR is connected to moisture, where more moisture in the atmosphere can increase the amount of radiation that is reflected back down to the surface, a positive DLR anomaly may indicate a higher moisture content in the atmosphere. This agrees with Figure 4.11c,d, as the positive and negative humidity and DLR anomalies coincide for both groups.

One would expect the DLR anomalies to be positive for both groups, as cyclones are related to the development of clouds that both reflect absorb the outgoing longwave radiation and emit it back to the surface. However, the low-θ_e group shows negative DLR anomalies in the study region. There are some possible explanations of this surprising result. For example, as the Arctic is generally a very cloudy area, a negative anomaly does not mean that clouds are absent, but rather that there are less clouds than the climatological cloudiness. As the climatology includes all winter days, both with and without cyclones present, the cyclones from the high-θ_e group can increase the climatological cloudiness. Further, the cyclones in the low-θ_e group are associated with a very dry atmosphere that can have a reduced formation of clouds in the study region. Another possible explanation is the low temperatures connected to the low-θ_e cyclones. As the outgoing longwave radiation is a function of temperature through the Stefan Boltzmann's Law (*Hartmann*, 2016), a lower temperature at the surface will decrease the amount of emitted longwave radiation from the surface to the atmosphere. This can result in less radiation being reflected/emitted back to the surface as DLR.

The daily evolutions of the turbulent heat flux and DLR anomalies show that the two groups have opposite preconditioned environments. Figure 4.14 shows the evolution of total turbulent heat flux (4.14a) and DLR (4.14b) anomalies from 4 days before to 4 days after genesis. The anomalies are given as the total radiation over the study

region to represent the total impact on the region, and are therefore given in Watt $[W]$. While the cyclones in the high-θ_e group (red) have their strongest turbulent heat flux anomaly at genesis day (day 0), the cyclones in the low-θ_e group (blue) have their strongest turbulent heat flux anomaly 1 day before genesis (day -1). The cyclones in both groups have their strongest anomalies in DLR on genesis day. Further, the turbulent heat flux anomalies are stronger than the DLR anomalies, indicating that the cyclones have a larger influence on the energy exchange between ocean and atmosphere compared to the downward emittance of longwave radiation from, for example, clouds. The differences between the two groups are significant both at genesis and several days before genesis, according to the bootstrap analysis. Both the DLR and turbulent heat flux evolutions show a strong preconditioning of the environment, with anomalous values for both groups up to 4 days before genesis day. This preconditioning of the environment agrees with the daily evolution of 2m temperature and specific humidity.
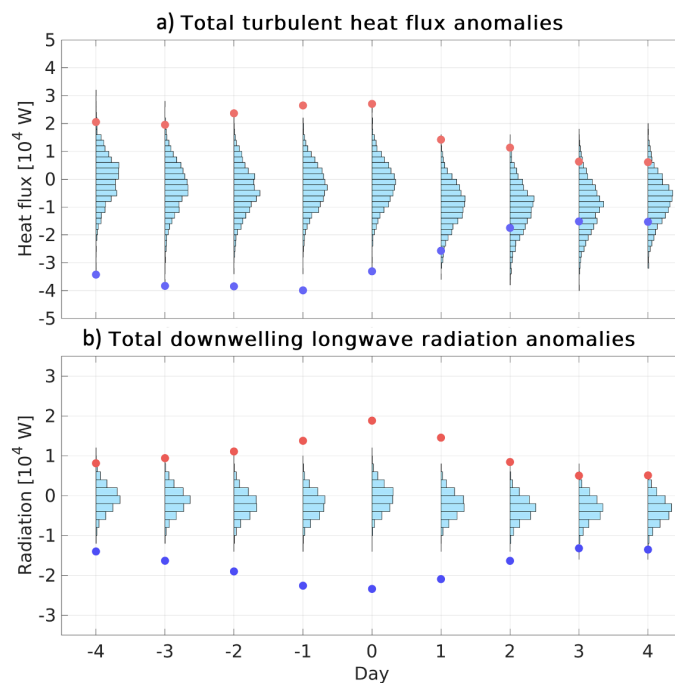

Figure 4.14: Daily evolution of the a) total turbulent heat flux $[W]$ and b) total DLR $[W]$ anomalies, from 4 days before genesis to 4 days after genesis, where day 0 is genesis. Histograms show the probability distribution estimated by performing a bootstrap resampling analysis. The high-θ_e (red) and low-θ_e (blue) anomalies are shown with dots for each day.

4.4.2 Precipitation and sea ice

Cyclones influence the local weather as they travel over the Arctic, and can in extreme cases cause storm surges, flooding, snowmelt and reduced sea ice (e.g., *Binder et al.*, 2017; *Dacre and Pinto*, 2020). We therefore want to investigate the impacts of the high-θ_e and low-θ_e groups on the Arctic climate, by looking at precipitation and sea ice.

Cyclones are associated with local precipitation along their paths, and we therefore

want to study the spatial coverage of precipitation for the two groups. Figure 4.15 shows maps of the precipitation anomalies for the low-θ_e (4.15a) and high-θ_e (4.15b) groups. The low-θ_e group shows weak total precipitation anomalies in the study region, with negative anomalies close to Greenland and Svalbard, and positive anomalies over northern Norway. Outside the study region, however, there are stronger precipitation anomalies, with negative anomalies over Iceland and western Norway, and positive anomalies at the southern tip of Greenland. The high-θ_e group shows positive anomalies of total precipitation in the study region, signifying more precipitation than climatology. This suggests that the cyclones belonging to the high-θ_e group result in increased precipitation over the study region, while the cyclones in the low-θ_e group have little impact on the total precipitation over the region. In addition, the high-θ_e group exhibits negative anomalies along southeast Greenland, thus displaying the same dipole structure as seen earlier. This dipole structure is less evident in the low-θ_e group map.

The amount of precipitation connected to each group depends on the precipitation type, i.e., whether it is large-scale or convective precipitation. The total precipitation anomalies are the sum of the large-scale (Figure 4.15c,d) and convective (Figure 4.15e,f) precipitation anomalies. The large-scale precipitation anomalies account for most of the total precipitation anomalies, with strong positive (weak negative) anomalies in the study region for the high-θ_e (low-θ_e) group. While the large-scale precipitation shows a nearly identical pattern as the total precipitation, the convective precipitation shows an opposite pattern, with negative (positive) anomalies in the study region for the high-θ_e (low-θ_e) group. This suggests that although there is less precipitation connected to the low-θ_e group than climatology, a larger fraction of the precipitation is related to convection. More convective precipitation means that the atmosphere is likely more vigorous for the cyclones in the low-θ_e group than the cyclones in the high-θ_e group, supporting the findings from Section 4.2. Conversely, while there is more large-scale precipitation than climatology connected to the high-θ_e group, there is less convective precipitation, suggesting that more of the precipitation is related to the formation of synoptic clouds than to convection.

The daily evolution of precipitation shows the strongest precipitation anomalies close to genesis day. Figure 4.16 shows the daily anomalies from the accumulated precipitation over the whole study region, given in total precipitation (4.16a), large-scale precipitation (4.16b) and convective precipitation (4.16c). The total precipitation is close to climatology at 3-4 days before genesis and 2-4 days after genesis, suggesting the cyclone-induced precipitation is more clustered around genesis day (day 0). This can be explained by precipitation typically being a local event and therefore varies a lot from area to area, which is also seen on the daily evolution maps (Figure C.5). On genesis day, the high-θ_e group shows a strong spike in total precipitation anomalies, with a positive anomaly of 0.7 m/day. The low-θ_e group, however, shows the strongest anomaly 1 day before genesis (day -1), with 0.2 m/day less precipitation than climatology. The strongest anomaly 1 day before genesis suggests that the group is connected to a preconditioned environment, consistent with previous findings. The large-scale precipitation exhibits a similar evolution as the total precipitation, but with stronger anomalies. This is especially clear on genesis day, when the high-θ_e group shows a pos-
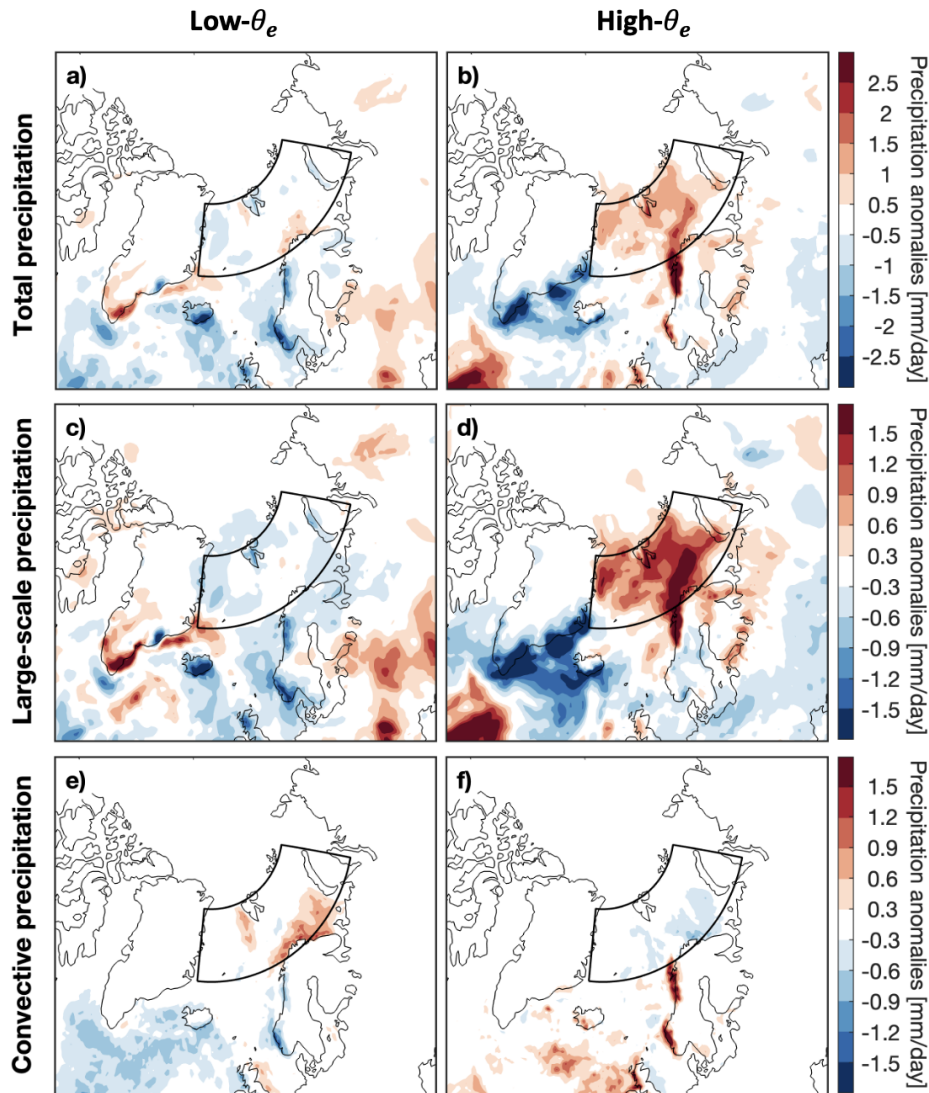
Figure 4.15: Maps of the precipitation anomalies [mm/day] for the low-θₑ (a,c,e) and high-θₑ (b,d,f) groups. a,b) Maps of the total precipitation anomalies, which are the sum of c,d) large-scale precipitation and e,f) convective precipitation. Red (blue) colours indicate more (less) precipitation than climatology.

itive anomaly of 0.85 m/day. The convective precipitation, however, is much smaller than the large-scale precipitation, with a positive anomaly of only 0.1 m/day for the low-θ_e group and negative anomaly of -0.15 m/day for the high-θ_e group. The opposite evolution between the convective precipitation and the large-scale precipitation explains why the large-scale precipitation anomalies are larger than the total precipitation anomalies. Close to genesis day, the differences between the two groups are significant, according to the bootstrap analysis.

As the cyclones influence the amount of precipitation in the area, we want to know the form of the precipitation that reaches the surface, which can be shown by the distribution between rain and snow. Figure 4.17a,b shows the snow/precipitation ratio for the low-θ_e (4.17a) and high-θ_e (4.17b) groups in absolute values. A value of 1 represents all precipitation falling as snow, while a value of 0 represents all precipitation
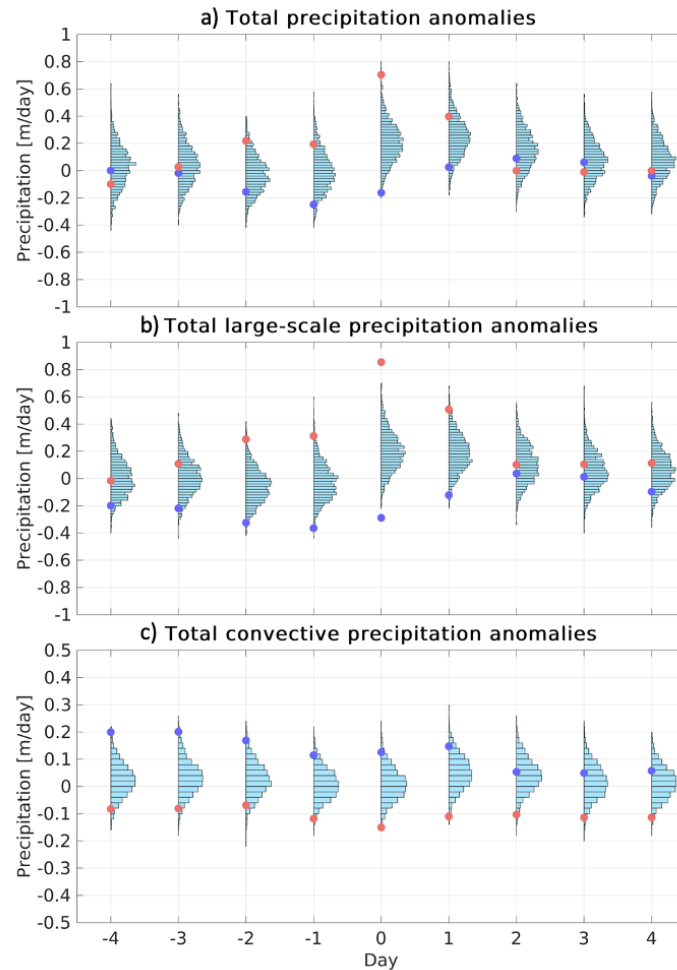
Figure 4.16: Daily evolution of the accumulated a) total precipitation [m/day] anomalies, which is the sum of b) large-scale precipitation and c) convective precipitation anomalies, from 4 days before genesis to 4 days after genesis, where day 0 is genesis. Histograms show the probability distribution estimated by performing a bootstrap resampling analysis. The high-θ_e (red) and low-θ_e (blue) anomalies are shown with dots for each day.

falling as rain. The map for the low-θ_e group shows that nearly all precipitation in the study region falls as snow, with a ratio of 0.9-1 over most of the area. The high-θ_e group, however, shows large areas with ratio below 0.5 in the study region, indicating that more than 50% of the precipitation falls as rain in this part of the region. The difference is largest close to Norway, likely due to warm and moist air being transported from the North Atlantic into the Arctic by large-scale systems.

The total snowfall anomalies for the two groups are consistent with the total precipitation anomalies in areas where most precipitation in the study region falls as snow. The two groups show positive and negative snowfall anomalies at different locations within the study region (Figure 4.17c,d), where the low-θ_e group (4.17c) shows more snowfall than climatology close to Norway while the high-θ_e group (4.17d) shows slightly less snowfall close to Norway. The spatial signatures in the snowfall anomalies concur with the precipitation anomalies and the snow/precipitation ratio. The positive (negative) anomalies seen on the northern part of the study region in the high-θ_e (low-θ_e) group

coincide well with the positive (negative) anomalies in the total precipitation map (Figure 4.15a,b) and are located at an area where all precipitation falls as snow (Figure 4.17a,b). Also, the negative anomalies in the southern part of the study region for the high-θ_e group do not coincide with the positive anomalies seen in the total precipitation map, as this is an area where the precipitation falls as rain.
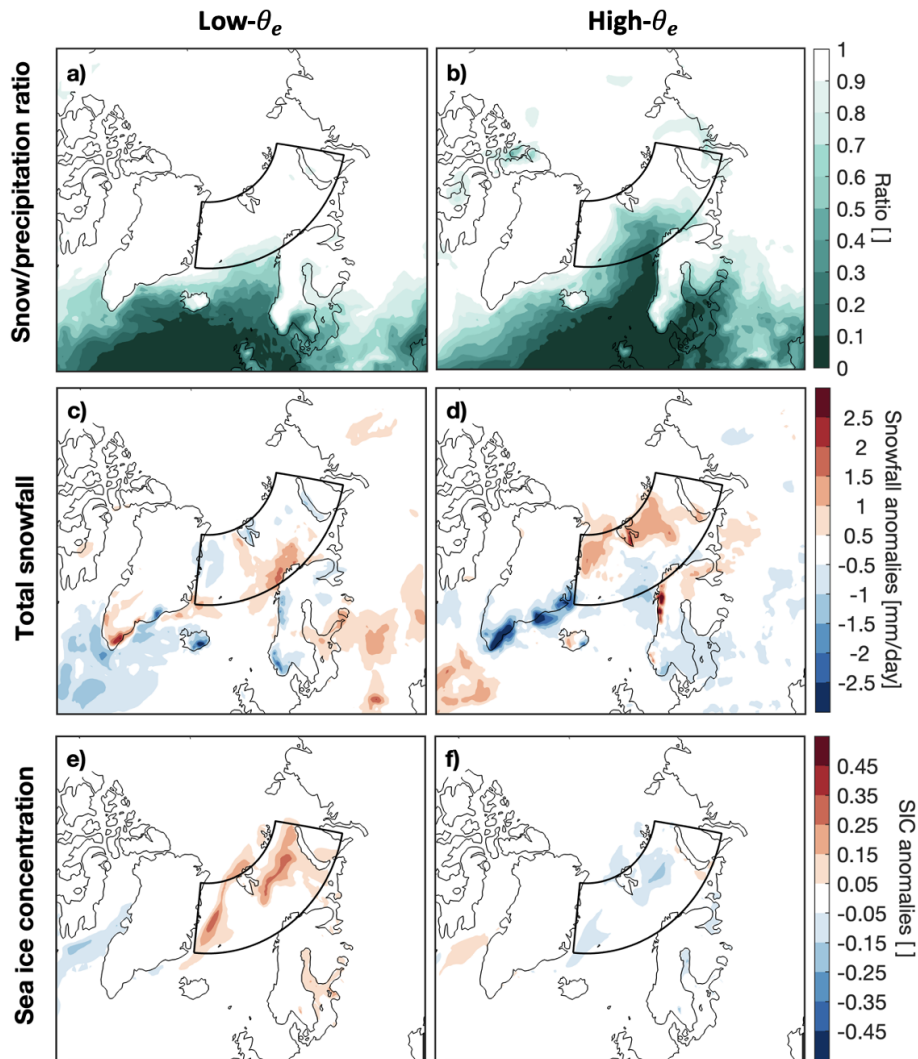

Figure 4.17: Maps of the a,b) snow/precipitation ratio [ ], c,d) snowfall anomalies [mm/day] and e,f) sea ice concentration (SIC) anomalies [ ] for the a,c,e) low-θ_e and b,d,f) high-θ_e groups. a,b) White colours indicate all precipitation falling as snow (ratio = 1), while the darkest shade of green indicates all precipitation falling as rain (ratio = 0). c-f) Red colours indicate more snowfall (higher SIC) than climatology while blue colours indicate less snowfall (lower SIC) than climatology for the total snowfall (SIC) maps.

The cyclone groups affect the sea ice concentration (SIC) in the Arctic, especially close to the sea ice edge. Figure 4.17e,f shows the SIC anomalies for the low-θ_e (4.17e) and high-θ_e (4.17f) groups. The maps show the ratio of SIC, where 1 is only sea ice and 0 is no sea ice. Cyclones are often assumed to be related to sea ice melt (e.g., *Blanchard-Wrigglesworth et al.*, 2022; *Graham et al.*, 2019; *Valkonen et al.*, 2021) with warm and moist air transported by the cyclones affecting the sea ice. This is supported by

the high-θ_e group, displaying reduced SIC in the study region. Conversely, the low-θ_e group shows a growth in SIC. A possible explanation is the anomalously low air temperature connected to this group that, if low enough, can support sea ice growth. Further, the cyclones can cause both a reduction and an increase in SIC based on the relative location of the cyclone, and they can redistribute the sea ice (*Clancy et al.*, 2022). The increase in sea ice along the edge could therefore be a redistribution of sea ice from the marginal ice zone in the north to the sea ice edge further south.

4.4.3   Summary of the opposing environmental impacts

The Arctic maps show opposite environments connected to the high-θ_e and low-θ_e groups (Figures 4.11-4.17). The positive (negative) temperature and humidity anomalies for the high-θ_e (low-θ_e) group are expected, based on the definition of the two groups. In winter, the ocean is warmer than the air above, causing an energy exchange from the ocean to the atmosphere. As the cyclones in the high-θ_e group are connected to warmer air temperatures, the temperature contrast between the atmosphere and ocean will be smaller, which may explain the weaker heat fluxes from ocean to atmosphere. The warmer temperatures may also explain why there is more rain than snow in the southern part of the study region compared to the cold cyclones in the low-θ_e group. Similarly, the colder air temperatures connected to the low-θ_e cyclones may result in a stronger temperature contrast between the atmosphere and the ocean, and therefore stronger heat fluxes from ocean to atmosphere. The bootstrap analysis shows that the two groups are significantly different from each other. Therefore, when studying the cyclones with the 10% highest and lowest θ_e, these cyclones show a significant impact on the Arctic region, which is not observed by composite analyses, such as the findings of *Madonna et al.* (2020) who studied all Arctic cyclones as one.

4.5   Summary

Through comparing the cyclones with the 10% highest θ_e (high-θ_e) and 10% lowest θ_e (low-θ_e), we see both similarities and differences between these two groups. The main results are listed below.

- Cyclones in both groups have a thermally direct circulation, with higher θ_e air rising and lower θ_e air sinking.

- The cyclones in the low-θ_e group have shallower but more vigorous isentropic overturning, while the cyclones in the high-θ_e group have deeper isentropic overturning but are less vigorous.

- The cyclones in the high-θ_e group are strongest at genesis but decay rapidly, while the cyclones in the low-θ_e group strengthen the first day before decaying.

- While the cyclones in the high-θ_e group have a lower SLP, the cyclones in the low-θ_e group have a larger heat release.

- The two groups are connected to opposite environments, with positive (negative) anomalies for the high-θ_e (low-θ_e) group for most variables both on genesis day and several days before genesis, suggesting preconditioning.

Chapter 5

Discussion

5.1 Possible energy sources for cyclogenesis

Our results in Chapter 4 have shown that the high-θ_e and low-θ_e cyclone groups have different characteristics. This may suggest that they are related to different energy sources for cyclogenesis, which may be connected to the location of where the cyclones originate. As briefly discussed in Section 4.1, the high-θ_e tracks and low-θ_e tracks cluster in different locations in the study region (Figure 4.1). The cyclones belonging to the low-θ_e group mostly have genesis along the sea ice edge, with the exception of some cyclones originating further south in the study region close to the Nordic countries and Russia. On the other hand, most of the cyclones belonging to the high-θ_e group originate in the northernmost part of the North Atlantic, especially in the southwest corner of the study region that is just southeast of Greenland.

As cyclones in the low-θ_e group are cold and dry, and cluster mostly along the sea ice edge, this may suggest that they are formed from baroclinicity induced by the sea ice edge. Cyclogenesis along the sea ice edge is frequently observed (chapter 4 in *Serreze and Barry*, 2005), where the interface between the warmer ocean and the colder sea ice creates a strong temperature contrast. This results in a strong horizontal temperature gradient that can be favourable for cyclogenesis (*Inoue and Hori*, 2011). Further, the anomalously low air temperatures both before and during cyclone genesis for the low-θ_e group can strengthen the ocean-sea ice temperature contrast by making the temperature over sea ice colder than normal. This enhanced temperature contrast can enhance the baroclinicity (assuming no changes in the atmospheric stability) needed for cyclones to form.

The cyclones in the high-θ_e group are warm and humid, and are mostly originating in the northernmost part of the North Atlantic and on the lee side of Greenland. Cyclones originating southeast of Greenland may be formed by the high orographic barrier in Greenland (chapter 4 in *Serreze and Barry*, 2005). The mountains can block the low-level westerly flow on their windward side and create a lower-level gradient on their lee side, needed for baroclinicity to form (*Tibaldi et al.*, 1990). The air descending on the lee side of the mountains can induce vorticity, and if the descending flow is strong enough, the fall in pressure results in a surface low (*Wallace et al.*, 2006). Cyclones created in this way typically have a warm core structure because of the adiabatic warm-

ing when the flow moves down the mountain. This supports the anomalously warm temperatures, but not the anomalously humid air, seen in the high-θ_e cyclones, as adiabatic warming is usually associated with dryness. Nevertheless, some of the high-θ_e cyclones may be created from a surface low induced by the Greenland mountains.

The cyclones in the high-θ_e group originating in the northernmost part of the North Atlantic have no clear source of a low-level baroclinicity present, but they can be the result of secondary genesis. Cyclones travelling from further south in the North Atlantic can influence the Arctic environment when they arrive, and can create a favourable environment for secondary genesis when they decay, as there would be a low pressure trough present in the area that leaves a trailing front for the Arctic cyclones to form (*Hakim and Patoux*, 2018). This is often seen at the eastern part of the North Atlantic storm track, partly coinciding with the study region. Also, cyclones originating further south and travelling into the Arctic transport warm and moist air along their paths. These cyclones at the end of their life cycles might therefore provide an appropriate warm and humid environment for secondary cyclogenesis. This is supported by the preconditioned warm and humid environment seen in the study region before cyclogenesis. In addition, cyclones created by secondary genesis have been found to deepen rapidly (*Parker*, 1998). As the cyclones in the high-θ_e group shows a more rapid deepening and decaying compared to the cyclones in the low-θ_e group, this further strengthens the suggestion that some of the high-θ_e cyclones are due to secondary genesis.

5.2 Relation between dipole pattern and large-scale regimes

Several of the anomaly maps show a dipole pattern, with positive (negative) anomalies in the study region and negative (positive) anomalies west/southwest of the study region for the high-θ_e (low-θ_e) group. This dipole pattern is seen in the anomaly maps for 2m temperature, specific humidity, downwelling longwave radiation (DLR), turbulent heat flux and precipitation (although less evident) (Figures 4.11, 4.13 and 4.15). Such a large-scale dipole pattern is also seen in *Rinke et al.* (2017), who studied composite anomalies of extreme low-pressure events during DJF winter from 1979-2015. They found positive temperature and DLR anomalies close to Svalbard and negative anomalies south of Greenland, consistent with our results. As cyclones only influence the local environment, the Arctic cyclones can only explain the anomalies seen in the study region. Therefore, the opposite anomalies seen southwest of the region (in the North Atlantic) need to be the result of some other atmospheric feature that have an opposite influence on the North Atlantic than the cyclones in the study region. This means that we cannot consider the Arctic cyclones as isolated features, but have to consider the atmospheric environment in the North Atlantic, too.

One possible explanation for the dipole pattern is that there is a high-θ_e cyclone and a low-θ_e cyclone present in the area at the same time, affecting the composites. For example, a high-θ_e cyclone would be present in the study region at the same time as a low-θ_e cyclone is present further southwest, resulting in positive anomalies in the study region and negative anomalies southwest of the region. Thus, the dates for all cyclones in the two groups have been cross-checked. Only three of the cyclones in the low-θ_e

group have a cyclone in the high-θ_e group arriving within a month after the low-θ_e cyclone. One of these cyclones has a high-θ_e cyclone created four days after the genesis of the low-θ_e cyclone. While this high-θ_e cyclone may affect the environment during the low-θ_e cyclone and vice versa, the cases are so few that they are unlikely to affect the composites.

A more likely explanation for the dipole pattern is large-scale flow patterns, such as the different phases of the North Atlantic Oscillation (NAO). Previous studies have found that the frequency and location of cyclones are related to the NAO pattern (e.g., *Bradbury*, 1958; *Pinto et al.*, 2009; *Rinke et al.*, 2017). A positive NAO correlates with a higher activity of North Atlantic cyclones, more southwest-northeast tilted storm track and Arctic warm extremes (*Gaffney et al.*, 2006; *Murto et al.*, 2022). This may be connected to the high-θ_e cyclones, as North Atlantic cyclones travelling further northward can facilitate a preconditioned warm environment, explaining the anomalously warm Arctic several days before cyclogenesis (Figure C.2, bottom row) and supporting the suggestion that some of these cyclones are created from secondary genesis. Conversely, the low-θ_e group can be related to a negative NAO, as a negative NAO is associated with more zonal North Atlantic cyclone tracks and cold temperature anomalies in the Arctic (*Gaffney et al.*, 2006; *Honda et al.*, 2009). As the North Atlantic cyclones have a more zonal direction, less heat and moisture will be transported into the Arctic by these cyclones, possibly explaining the cold temperatures seen up to several days before cyclogenesis for the low-θ_e cyclones (Figure C.2, top row).

However, large-scale conditions in the Arctic/North Atlantic are related to jet and weather regimes, and the NAO alone is too simplistic to represent these conditions well. The East Atlantic pattern (EA) is also important to consider, and *Woollings et al.* (2010) connected three preferred positions of the winter jet to the NAO and EA patterns. They found that large-scale patterns connected to the southern jet are similar to a negative NAO, patterns connected to the central jet are similar to a positive EA and patterns connected to the northern jet are similar to a negative EA. However, they concluded that it is not always sufficient to consider the NAO and EA patterns when studying jet stream variability. By adding a mixed jet as an extra jet regime, *Madonna et al.* (2017) connected the four jet regimes to four weather regimes, including their associated blocking patterns. They also compared the four jet regimes with the NAO/EA indices and found that while the jet regimes cluster in different phases of NAO/EA, several of the regimes cannot be clearly distinguished by one specific NAO/EA phase. Although the NAO/EA indices can give a simplistic view of the region, they are not a direct measure of the different jet regimes. Instead, weather regimes and jet patterns would provide a better picture of the large-scale variability in the North Atlantic. As the jet steers the flow, jet regimes can influence where most North Atlantic cyclones travel. Further, the weather regimes are closely related to atmospheric blocking that can also steer the cyclones. Previous studies have found that northward cyclone tracks often have a block east/northeast of the cyclones (e.g., *Booth et al.*, 2017). The jet and weather regimes can therefore influence the North Atlantic cyclone tracks and cyclone activity.

The dipole pattern seen in the high-θ_e and low-θ_e groups may be related to specific

jet and weather regimes. The cyclones in the high-θ_e group display warm and moist anomalies in the study region and cold and dry anomalies in the North Atlantic. They are likely associated with warm and moist air being advected into the study region from appropriate weather and jet regimes, and in some cases from the presence of North Atlantic cyclones. As the zonal regime has been found to be the dominant weather regime for serial cyclone clustering in high (65°) latitudes (*Hauser et al.*, 2023), a possible large-scale condition for the high-θ_e cyclones is the zonal regime and the central jet. Conversely, the cyclones in the low-θ_e group display cold and dry anomalies in the study region and warm and moist anomalies in the North Atlantic. They are likely associated with appropriate weather and jet regimes inhibiting warm and moist air to travel into the Arctic. A possible large-scale condition for the low-θ_e cyclones is therefore the southern jet and the Greenland anticyclone weather regime. Both groups show a preconditioning of the environment up to a few days before genesis, with positive (negative) temperature, humidity, and heat flux anomalies for the high-θ_e (low-θ_e) group, supporting their relation to large-scale systems. While the cyclones are connected to strong anomalous environments in the Arctic, this does not necessarily imply that the cyclones themselves have a strong impact, but rather that they can have been created during strong anomalous environments caused by large-scale systems.

Chapter 6

Conclusions

In this thesis, we have assessed the genesis and early development of cyclones born in the Arctic. We have retrieved information on the atmospheric and surface conditions through the lifetime of the cyclones using ERA5 reanalysis data. The cyclone tracks are identified and tracked by the Melbourne tracking scheme, and only cyclones with genesis in the winter months (DJF) during the period 1979-2020 are included. The cyclones are studied using an isentropic framework that is suitable for studying the overturning circulation and energy cycle of cyclones, and simplifies the analysis of the complex structure of cyclone overturning by grouping the air parcels based on their equivalent potential temperature, θ_e. As Arctic cyclones exhibit large variability in their θ_e (compared to the variability of midlatitude cyclones), we have chosen the cyclones with the 10% highest and 10% lowest θ_e, naming the groups high-θ_e and low-θ_e, respectively. Studying these two groups, we have aimed to answer the following three research questions.

Do warm and moist cyclones exhibit a different dynamical development from cold and dry cyclones?

Cyclones in both groups show a thermally direct circulation, with warm/moist air rising in rapid, near-adiabatic motion and cold/dry air sinking more slowly and more affected by diabatic processes. However, the overturning circulation of the two groups differs in strength, extent and evolution. For the first 24 hours after genesis, the cyclones in the high-θ_e group have a vertically deeper but less vigorous overturning circulation, a generally lower sea level pressure (SLP), and a more gentle mean θ_e gradient compared to the cyclones in the low-θ_e group (Figures 4.2-4.5 and 4.7). To assess whether the group composites are representative of the individual cyclones, we studied the distribution across all cyclones in each group for key characteristics such as the streamfunction, maximum streamfunction strength, SLP and heat release (ΔQ), using a kernel density estimate. The highest probabilities of occurrence coincide with most of the composites and group medians, giving an indication that the composites and group medians represent reasonably well the overturning circulation and evolution of any given cyclone (Figures 4.6, 4.9 and 4.10). Additionally, while there is large variability within each group, the two groups differ significantly at the start of evolution and become more similar to each other over time (Figure 4.3). This indicates that both groups converge towards some climatological environment, where the cyclones in the low-θ_e

group evolve towards higher θ_e and the cyclones in the high-θ_e group evolve towards lower θ_e.

What are the differences in the energy cycle of warm and moist cyclones compared to cold and dry cyclones?

The strength and evolution of the energy cycle differ between the cyclones in the two groups. As mentioned, the high-θ_e group has overall deeper cyclones (as measured by central SLP) than the low-θ_e group. However, this difference decreases with time after genesis as the cyclones in the low-θ_e group decrease in SLP for the first 36 hours, while the cyclones in the high-θ_e group mostly increase in SLP during the life cycle (Figure 4.7). Further, the energy cycle is related to the heat released by and vigour of the overturning circulation, which can be estimated by the streamfunction (Figure 4.5). The area of the streamfunction indicates the amount of heat that is released during the circulation (shown by ΔQ), while the strength of the streamfunction indicates the vigour of the overturning circulation (shown by maximum streamfunction strength). The cyclones in the low-θ_e group have both greater maximum streamfunction strength and larger ΔQ than the cyclones in the high-θ_e group during most of the life cycle (Figure 4.8). While the cyclones in the low-θ_e group increase in maximum streamfunction ΔQ during the first day, the cyclones in the high-θ_e group decrease.

Do warm and moist cyclones and cold and dry cyclones have different impacts on the Arctic region?

The cyclones in the two groups have different impacts on the Arctic region. The cyclones in the high-θ_e group are related to a warmer and moister atmosphere with weaker turbulent heat fluxes and stronger downwelling longwave radiation (DLR) in the study region, while the cyclones in the low-θ_e group have a colder and drier atmosphere with stronger turbulent heat fluxes and weaker DLR compared to climatology (Figures 4.11 and 4.13). The higher (lower) temperature and humidity for the high-θ_e (low-θ_e) cyclones are expected, due to the definition of the two groups being based on near-surface θ_e. Further, the cyclones in the high-θ_e group are associated with more precipitation and snowfall, while the cyclones in the low-θ_e group are associated with less precipitation but larger snow fraction in the region (Figures 4.15 and 4.17). The large-scale precipitation accounts for most of the total precipitation connected to the high-θ_e group, while convective precipitation accounts for most of the precipitation connected to the low-θ_e group. Interestingly, while the cyclones in the high-θ_e group are associated with a lower sea ice concentration (SIC), the cyclones in the low-θ_e group are associated with in a higher SIC. Despite relatively small sample sizes, differences between the impacts associated with the two groups are meaningful according to the bootstrap analyses (Figures 4.12, 4.14 and 4.16).

Future Work and Outlook

We propose further research on the development of Arctic cyclones and their relation to large-scale systems. Most of the anomaly maps (temperature, humidity, turbulent heat flux, DLR, precipitation) show a dipole pattern, with positive (negative) anomalies

in the study region and negative (positive) anomalies west/southwest of the study region for the high-θ_e (low-θ_e) group (Figures 4.11, 4.13 and 4.15). The temperature and DLR also show a negative (positive) anomaly northeast of the study region, resulting in a tripole pattern. These patterns are seen up to several days before genesis, indicating a preconditioned environment and suggesting that the cyclones in the two groups are connected to large-scale systems, such as specific weather and jet regimes. Studying the distribution of different jet or weather regimes within each group may reveal if one regime is more frequently observed than the others and potentially preconditioning the atmospheric environment for the cyclones in this group.

Some of the cyclones were excluded because of an unusual SLP evolution (see Appendix A). We therefore propose a comparison of these results using another tracking scheme, which could reveal whether the excluded cyclones are due to the algorithm or due to other features, and could indicate the validity of the results.

While there have been a lot of studies about midlatitude cyclones, fewer studies have focused on the dynamics and development of cyclones originating in the Arctic. This thesis contributes to a better understanding of Arctic cyclones through identifying how the thermodynamic characteristics of the cyclones relate to their dynamical development and their impacts on the Arctic region. The cyclones in the high-θ_e and low-θ_e groups differ clearly in the strength and shape of the overturning circulation and show opposite impacts on the Arctic. These results contribute to the sustainable development goals (SDG) 14 and 15; Life below water and Life on land, respectively. Cyclones are important for the local weather and affect both the atmosphere and the surface. For example, the cyclones in the high-θ_e group are related to increased temperatures and precipitation, and such cyclones may in extreme cases result in severe warming, storm surges and flooding (SDG15). The cyclones in the low-θ_e group, however, are related to colder temperatures and less precipitation and may therefore result in Arctic cold extremes. Further, cyclones in both groups are related to a change in energy exchange between ocean and atmosphere, affecting the sea surface temperature, and to a change in sea ice concentration. These changes may affect ocean salinity and stratification, which has implications for ocean conditions and for marine life (SDG14). These results also contribute to SDG 13; Climate action, as cyclones are an important part of the climate system and can result in extreme events. Thus, research on the development and impact of Arctic cyclones can contribute to increased understanding of the Arctic climate system.

Appendix A

Cyclone tracks

After a review of the sea level pressure (SLP) evolution for each cyclone, some of the cyclones have been excluded from the groups to make the results cleaner (Figures A.1 and A.2). 9 cyclones in the low-θ_e group and 3 cyclones in the high-θ_e group show the lowest SLP value at the end of their life cycles (highlighted in pink), and are therefore excluded. This means that the low-θ_e and high-θ_e groups consist of 29 and 35 cyclones, respectively. Some of the cyclones have their lowest SLP at genesis (highlighted in green), indicating the cyclones are already at their strongest when the tracking of the cyclones started. As this evolution does not interfere with our focus of genesis and early development in this thesis, these cyclones are included in the analysis. 14 of the cyclones in the high-θ_e group and 7 of the cyclones in the low-θ_e group are classified in this group.
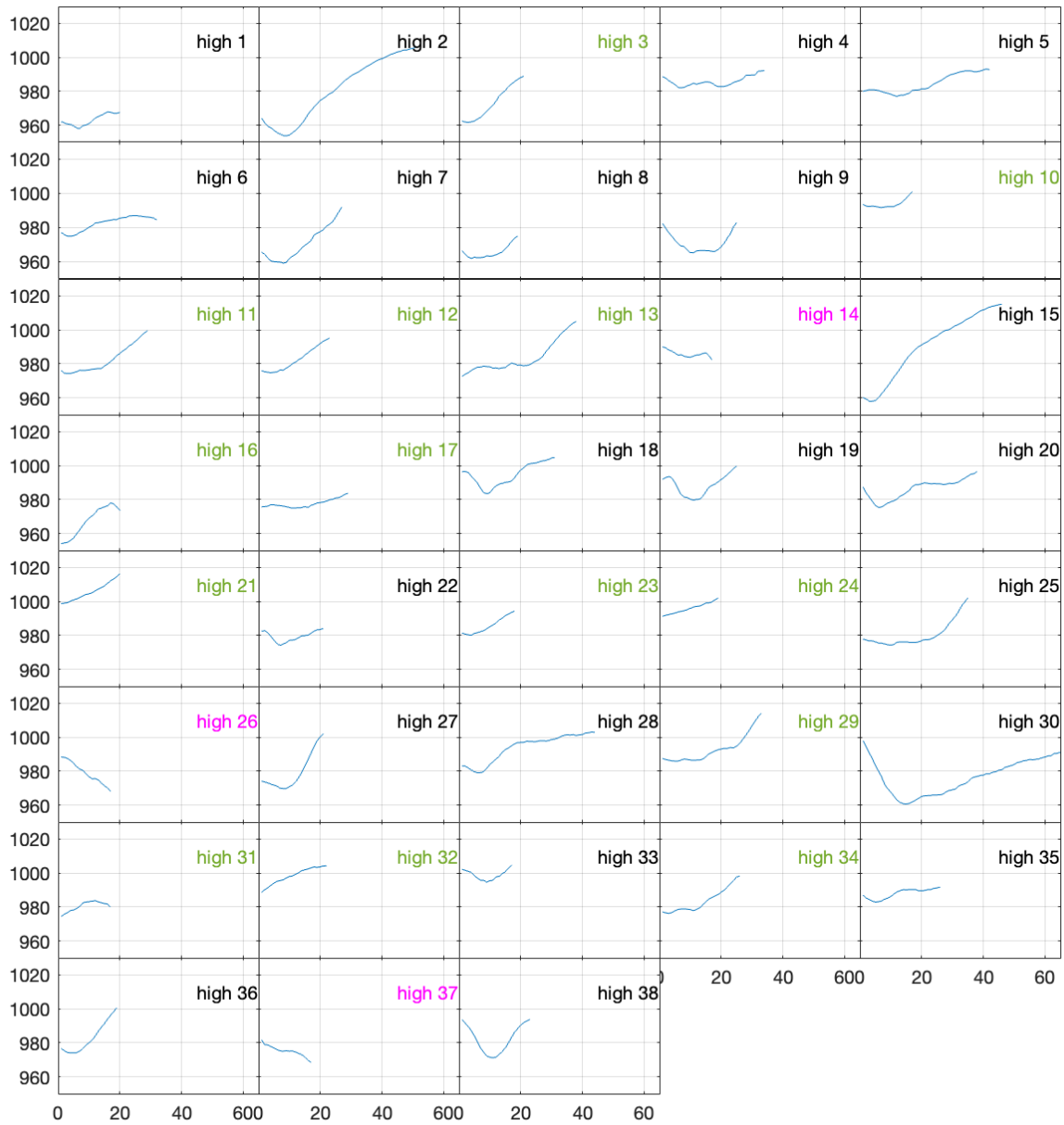
Figure A.1: Sea level pressure (SLP) evolution of each individual cyclone in the high-θ_e group. Cyclones highlighted in pink have their lowest SLP at the end of the life cycle and are therefore excluded. Cyclones highlighted in green have lowest SLP at genesis, but are included in the group. The high-θ_e group consists therefore of 35 cyclones.
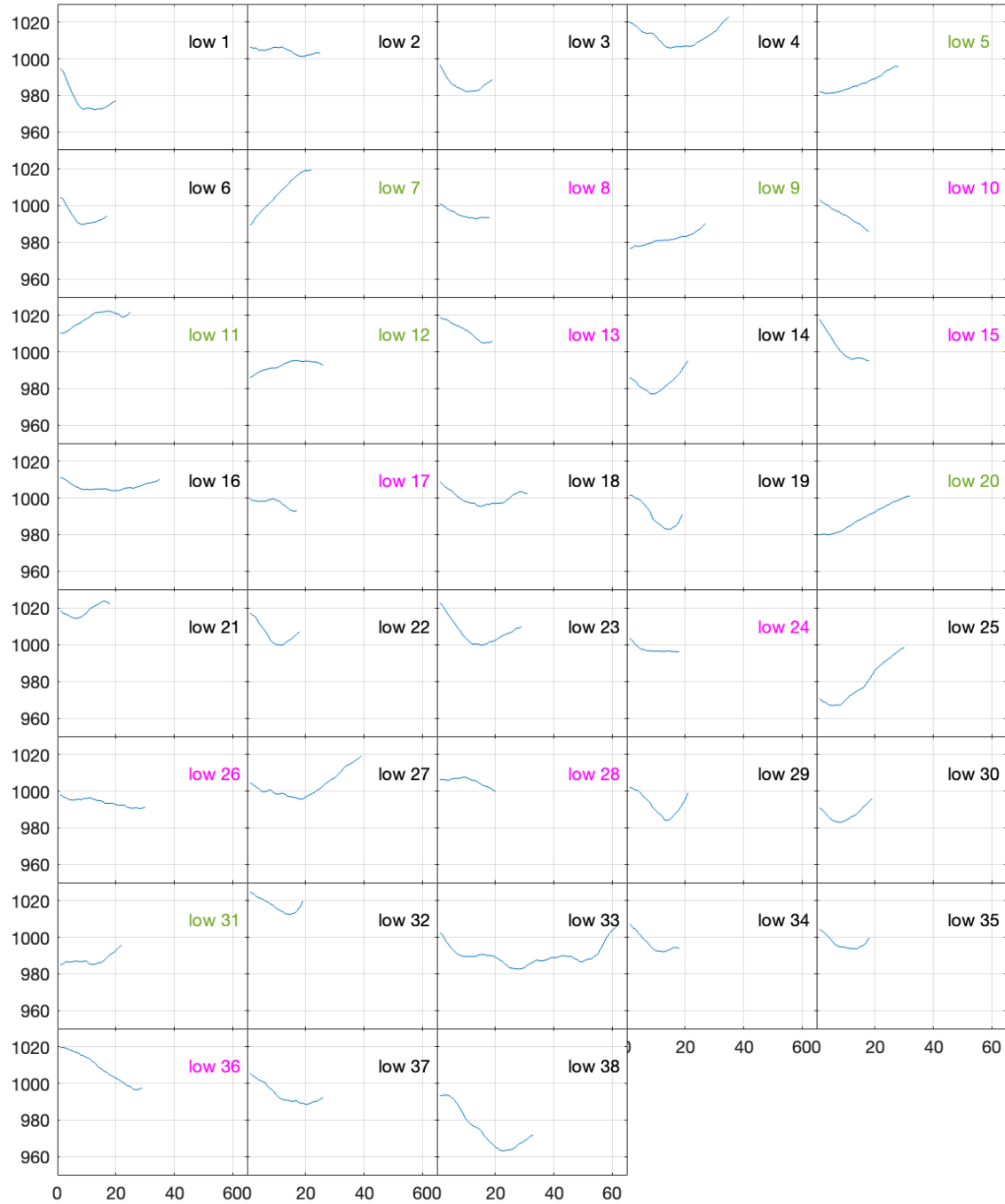
Figure A.2: Similar to Figure A.1, but for the low-θ_e group. The low-θ_e group consists of 29 cyclones.

Appendix B

Isentropic analysis
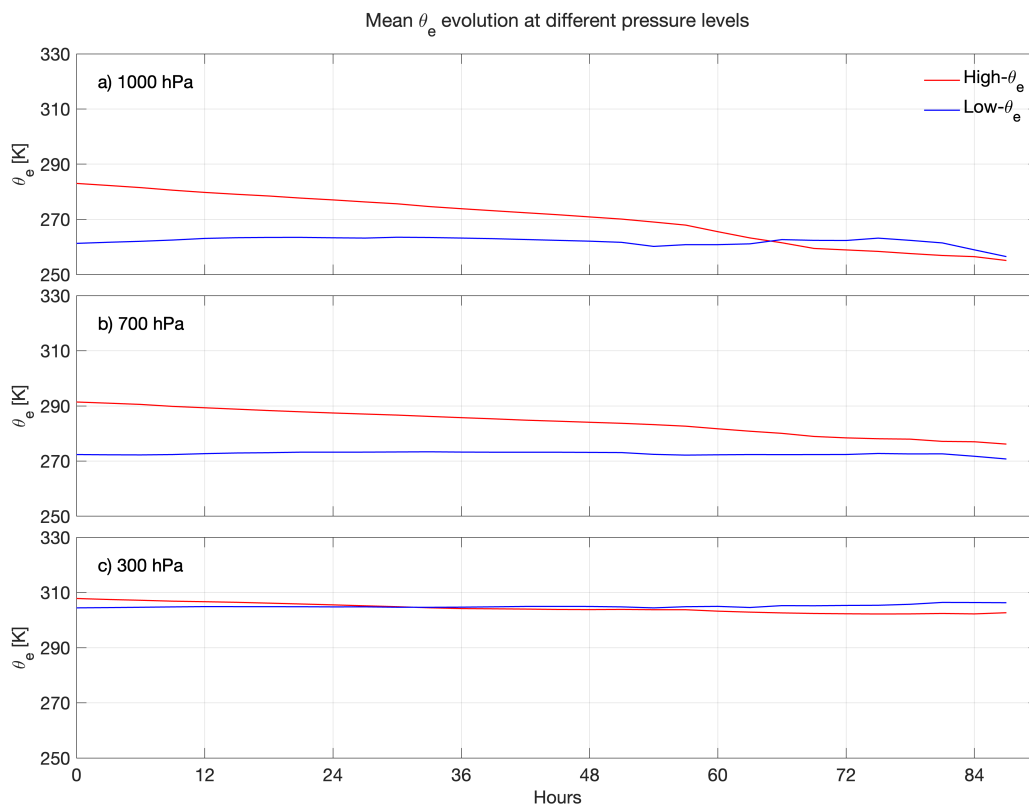
Figure B.1: Evolution of the mean θ_e for the high-θ_e (red) and low-θ_e (blue) groups at three pressure levels: a) At surface (1000hPa), b) in the middle of the troposphere (700hPa), and c) near the top of the troposphere (300hPa).
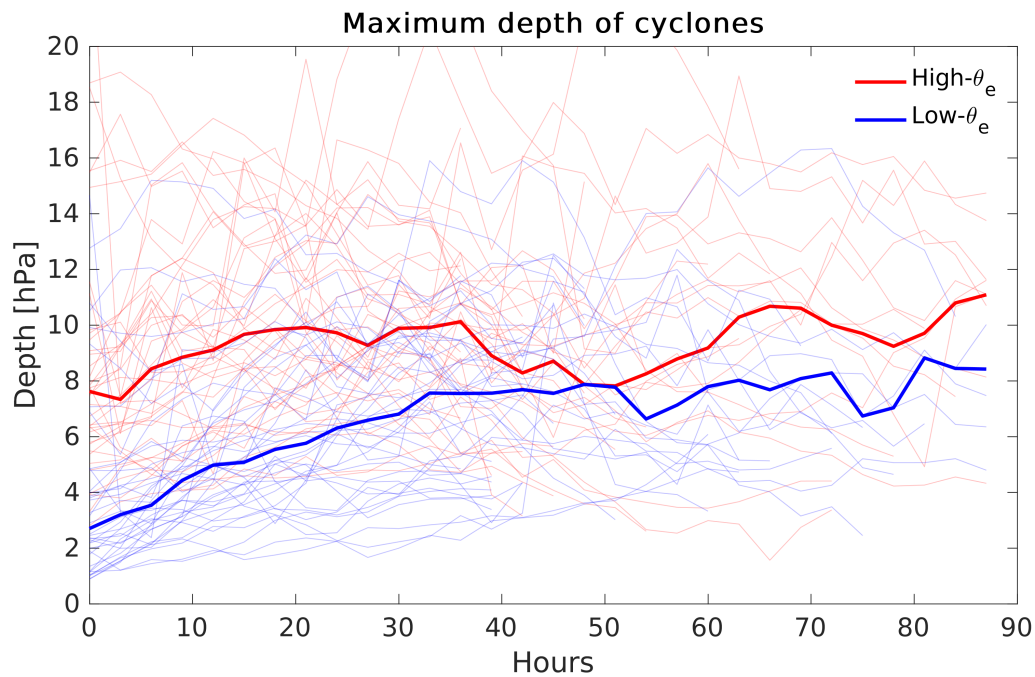
Figure B.2: Evolution of the cyclone depth for the high-θ$_e$ (red) and low-θ$_e$ (blue) groups. The individual cyclones are shown as thin lines, while the group median is shown with a thicker line.
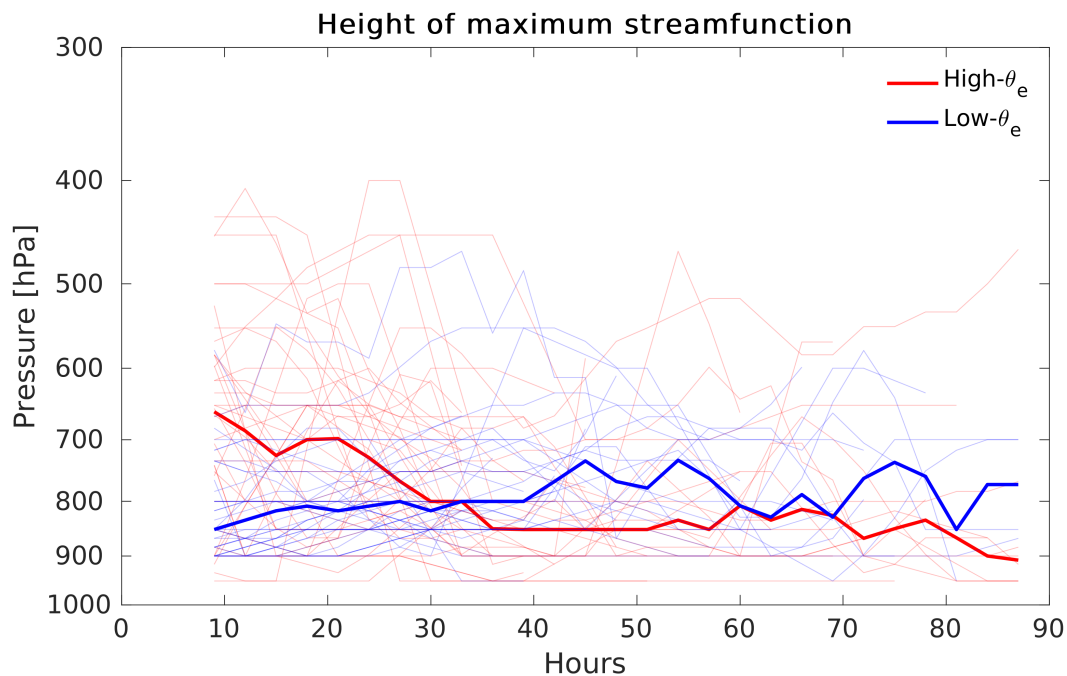

Figure B.3: Evolution of the height of the maximum streamfunction strength for the high-θ$_e$ (red) and low-θ$_e$ (blue) groups. Thin lines represent each individual cyclone, while the group median is shown with a thicker line. A running mean of 6 hours is applied to smooth the results, resulting in the first time step to be at 9 hours after genesis (first time step of streamfunction is at 6 hours after genesis and the data is 3-hourly spaced).
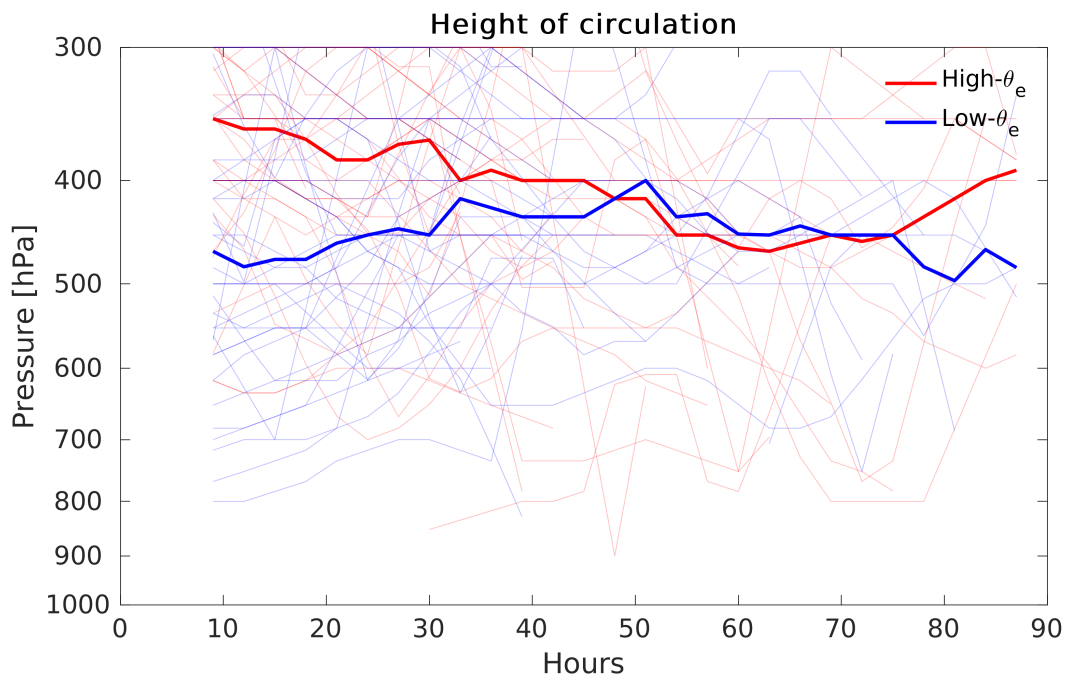
Figure B.4: Similar to Figure B.3, but showing the evolution of the height of the streamfunction.
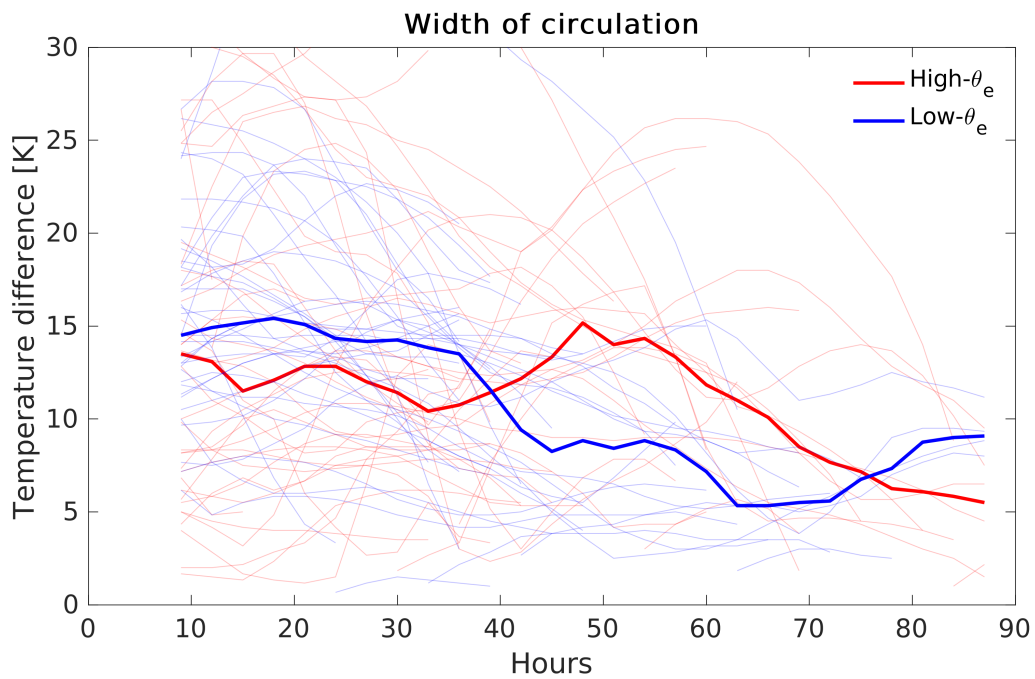

Figure B.5: Similar to Figure B.3, but showing the evolution of the width of the streamfunction.
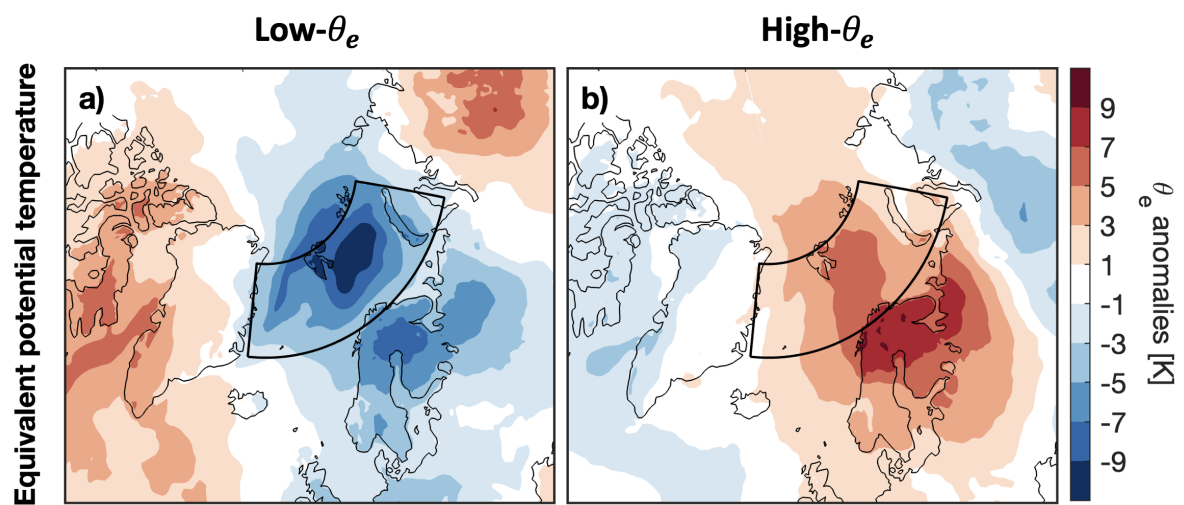
Appendix C

Arctic environment

Figure C.1: Maps of the equivalent potential temperature (θ_e) anomalies [K] for the a) low-θ_e and b) high-θ_e groups. The black contour shows the study region. Red colours indicate a warmer and moister atmosphere than climatology while blue colours indicate a colder and drier atmosphere than climatology.
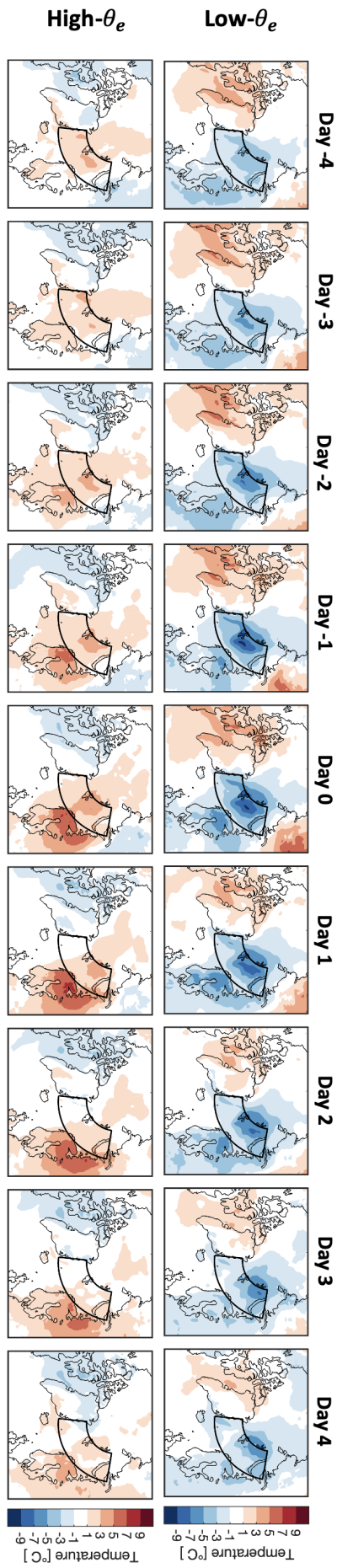
Figure C.2: Daily evolution of 2m temperature anomalies [K] for the high-θ_e and low-θ_e groups, from 4 days before genesis (day -4) to 4 days after genesis (day 4). The black contour shows the study region. Genesis day (day 0) is also shown in Figure 4.11a,b. Red (blue) colours indicate a warmer (colder) atmosphere than climatology.
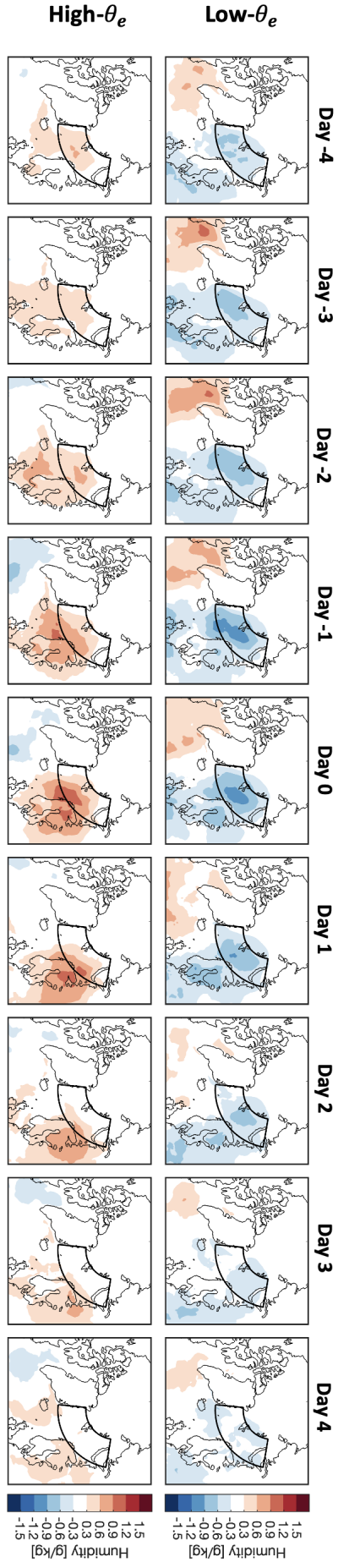
Figure C.3: Similar as Figure C.2, but for specific humidity anomalies [g/kg]. Genesis day (day 0) is also shown in Figure 4.11c,d. Red (blue) colours indicate a moister (drier) atmosphere than climatology.
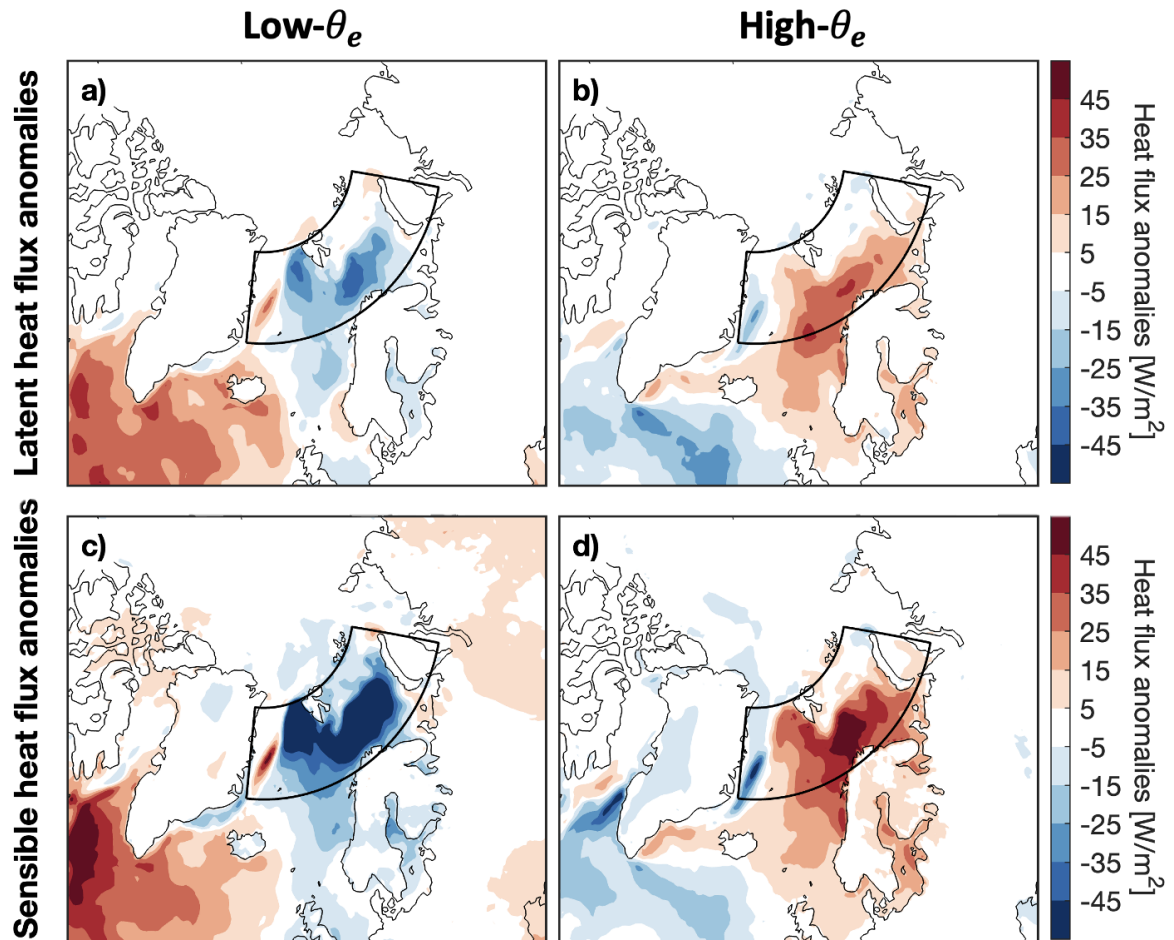
Figure C.4: Maps of the a,b) latent and c,d) sensible heat flux anomalies $[W/m^2]$ for the a,c) low-θ_e and b,d) high-θ_e groups. The black contour shows the study region. Red (blue) colours indicate less (more) heat flux from the ocean to the atmosphere compared to climatology.
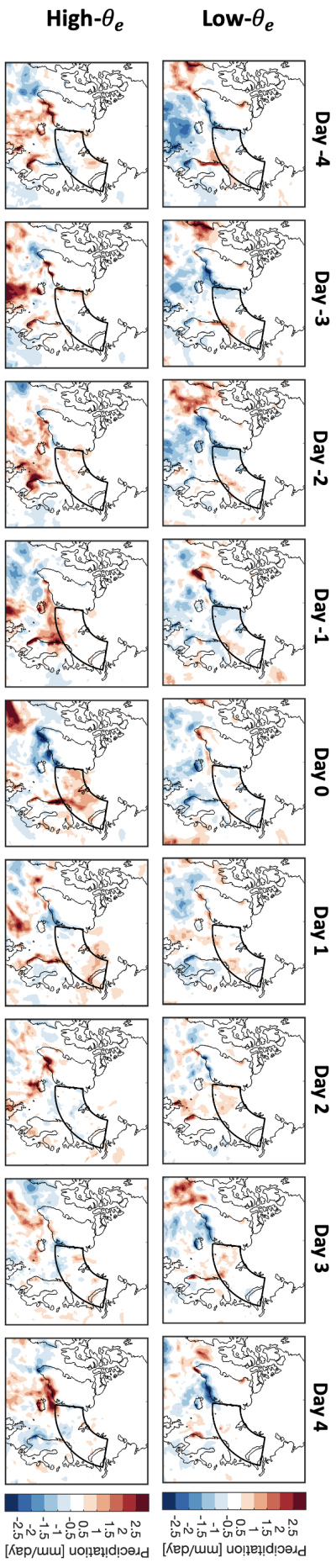
Figure C.5: Similar as Figure C.2, but for total precipitation anomalies [mm/day]. Genesis day (day 0) is also shown in Figure 4.15a,b. Red (blue) colours indicate more (less) total precipitation than climatology.

Bibliography

Aue, L., T. Vihma, P. Uotila, and A. Rinke (2022), New insights into cyclone impacts on sea ice in the atlantic sector of the arctic ocean in winter, *Geophysical Research Letters*, *49*(22), doi:10.1029/2022GL100051. 1.2

Bengtsson, L., K. I. Hodges, and E. Roeckner (2006), Storm tracks and climate change, *Journal of climate*, *19*(15), 3518–3543. 1.3

Binder, H., M. Boettcher, C. M. Grams, H. Joos, S. Pfahl, and H. Wernli (2017), Exceptional air mass transport and dynamical drivers of an extreme wintertime arctic warm event, *Geophysical Research Letters*, *44*(23), 12,028–12,036, doi: 10.1002/2017GL075841. 1, 1.2, 4.4.2

Bintanja, R., K. V. D. Wiel, E. C. V. D. Linden, J. Reusen, L. Bogerd, F. Krikken, and F. M. Selten (2020), Strong future increases in arctic precipitation variability linked to poleward moisture transport, doi:10.1126/sciadv.aax6869. 1.3

Bjerknes, J. (1919), On the structure of moving cyclones, *Monthly Weather Review*, *47*(2), 95–99, doi:10.1175/1520-0493(1919)47<95:OTSOMC>2.0.CO;2. 2

Bjerknes, J., and H. Solberg (1922), Life cycle of cyclones and the polar front theory of atmospheric circulation, *Geofysisks Publikationer*, *3*, 1–18. 2

Blanchard-Wrigglesworth, E., M. Webster, L. Boisvert, C. Parker, and C. Horvat (2022), Record arctic cyclone of january 2022: Characteristics, impacts, and predictability, *Journal of Geophysical Research: Atmospheres*, *127*(21), doi:10.1029/2022JD037161. 1, 1.2, 4.4.2

Boisvert, L. N., A. A. Petty, and J. C. Stroeve (2016), The impact of the extreme winter 2015/16 Arctic cyclone on the Barents-Kara Seas, *Monthly Weather Review*, *144*(11), 4279–4287, doi:10.1175/MWR-D-16-0234.s1. 1, 1.2

Booth, J. F., E. Dunn-Sigouin, and S. Pfahl (2017), The relationship between extratropical cyclone steering and blocking along the north american east coast, *Geophysical Research Letters*, *44*(23), 11,976–11,984, doi:10.1002/2017GL075941. 5.2

Boé, J., A. Hall, and X. Qu (2009), September sea-ice cover in the arctic ocean projected to vanish by 2100, *Nature Geoscience*, *2*(5), 341–343, doi:10.1038/ngeo467. 1.3

Bradbury, D. L. (1958), On the behavior patterns of cyclones and anticyclones as related to zonal index, *Bulletin of the American Meteorological Society*, *39*(3), 149–151, doi: 10.1175/1520-0477-39.3.149. 5.2

Brown, N. J., C. Mauritzen, C. Li, E. Madonna, P. E. Isachsen, and J. H. Lacasce (2023), Rapid response of the norwegian atlantic slope current to wind forcing, *Journal of Physical Oceanography*, *53*(2), 389–408, doi:10.1175/JPO-D-22-0014.1. 1

Butler, A. H., D. W. Thompson, and R. Heikes (2010), The steady-state atmospheric circulation response to climate change-like thermal forcings in a simple general circulation model, *Journal of Climate*, *23*(13), 3474–3496, doi:10.1175/2010JCLI3228. 1. 1.3

Catto, J. L., L. C. Shaffrey, and K. I. Hodges (2011), Northern hemisphere extratropical cyclones in a warming climate in the higem high-resolution climate model, *Journal of Climate*, *24*(20), 5336–5352, doi:10.1175/2011JCLI4181.1. 1.3

Chang, E. K. M., S. Lee, and K. L. Swanson (2002), Storm track dynamics, *Journal of Climate*, *15*(16), 2163–2183, doi:10.1175/1520-0442(2002)015<02163:STD>2.0.CO;2. 3.1

Chen, Y.-C. (2017), A tutorial on kernel density estimation and recent advances, *Biostatistics and Epidemiology*, *1*(1), 161–187, doi:10.1080/24709360.2017.1396742. 4.2.5

Clancy, R., C. M. Bitz, E. Blanchard-Wrigglesworth, M. C. Mcgraw, and S. M. Cavallo (2022), A cyclone-centered perspective on the drivers of asymmetric patterns in the atmosphere and sea ice during arctic cyclones, *Journal of Climate*, *35*(1), 73–89, doi:10.1175/JCLI-D-21. 4.4.2

Dacre, H. F., and J. G. Pinto (2020), Serial clustering of extratropical cyclones: a review of where, when and why it occurs, *npj Climate and Atmospheric Science*, *3*(1), doi:10.1038/s41612-020-00152-9. 1, 2, 4.4.2

Day, J. J., and K. I. Hodges (2018), Growing land-sea temperature contrast and the intensification of arctic cyclones, *Geophysical Research Letters*, *45*(8), 3673–3681, doi:10.1029/2018GL077587. 1.3

Eady, E. T. (1949), Long waves and cyclone waves, *Tellus*, *1*(3), 33–52, doi:10.3402/tellusa.v1i3.8507. 2

Fang, J., O. Pauluis, and F. Zhang (2017), Isentropic analysis on the intensification of hurricane edouard (2014), *Journal of the Atmospheric Sciences*, *74*(12), 4177–4197, doi:10.1175/JAS-D-17-0092.1. 3.3, 3.4, 3.4

Fang, J., O. Pauluis, and F. Zhang (2019), The thermodynamic cycles and associated energetics of hurricane edouard (2014) during its intensification, *Journal of the Atmospheric Sciences*, *76*(6), 1769–1784, doi:10.1175/JAS-D-18-0221.1. 3.4, 3.4

Fearon, M. G., J. D. Doyle, D. R. Ryglicki, P. M. Finocchio, and M. Sprenger (2021), The role of cyclones in moisture transport into the arctic, *Geophysical Research Letters*, *48*(4), doi:10.1029/2020GL090353. 1.2

Gaffney, S. J., A. W. Robertson, P. Smyth, S. J. Camargo, and M. Ghil (2006), Probabilistic clustering of extratropical cyclones using regression mixture models, *Climate Dynamics*, *29*, 423–440, doi:10.1007/s00382-007-0235-z. 5.2

Graham, R. M., L. Cohen, A. A. Petty, L. N. Boisvert, A. Rinke, S. R. Hudson, M. Nicolaus, and M. A. Granskog (2017), Increasing frequency and duration of arctic winter warming events, *Geophysical Research Letters*, *44*(13), 6974–6983, doi: 10.1002/2017GL073395. 1

Graham, R. M., P. Itkin, A. Meyer, A. Sundfjord, G. Spreen, L. H. Smedsrud, G. E. Liston, B. Cheng, L. Cohen, D. Divine, I. Fer, A. Fransson, S. Gerland, J. Haapala, S. R. Hudson, A. M. Johansson, J. King, I. Merkouriadi, A. K. Peterson, C. Provost, A. Randelhoff, A. Rinke, A. Rösel, N. Sennéchael, V. P. Walden, P. Duarte, P. Assmy, H. Steen, and M. A. Granskog (2019), Winter storms accelerate the demise of sea ice in the atlantic sector of the arctic ocean, *Scientific Reports*, *9*(1), doi:10.1038/s41598-019-45574-5. 4.4.2

Hakim, G., and J. Patoux (2018), *Weather: A concise introduction*, 1 ed., Cambridge University Press, Cambridge. 1.2, 2, 5.1

Hartmann, D. L. (2016), Chapter 2 - the global energy balance, in *Global Physical Climatology (Second Edition)*, edited by D. L. Hartmann, second edition ed., pp. 25–48, Elsevier, Boston, doi:https://doi.org/10.1016/B978-0-12-328531-7.00002-5. 1.1, 3.3, 3.3, 4.4.1

Hartmuth, K., L. Papritz, M. Boettcher, and H. Wernli (2023), Arctic seasonal variability and extremes, and the role of weather systems in a changing climate, *Geophysical Research Letters*, *50*(8), doi:10.1029/2022GL102349. 1.3

Harvey, B. J., L. C. Shaffrey, and T. J. Woollings (2015), Deconstructing the climate change response of the northern, *Climate Dynamics*, *45*, 2847–2860, doi:10.1007/s00382-015-2510-8. 1.3

Hauser, S., S. Mueller, X. Chen, T. C. Chen, J. G. Pinto, and C. M. Grams (2023), The linkage of serial cyclone clustering in western europe and weather regimes in the north atlantic-european region in boreal winter, *Geophysical Research Letters*, *50*(2), doi:10.1029/2022GL101900. 5.2

Hawcroft, M. K., L. C. Shaffrey, K. I. Hodges, and H. F. Dacre (2012), How much northern hemisphere precipitation is associated with extratropical cyclones?, *Geophysical Research Letters*, *39*(24), doi:10.1029/2012GL053866. 1

Hay, S., M. D. Priestley, H. Yu, J. L. Catto, and J. A. Screen (2023), The effect of arctic sea-ice loss on extratropical cyclones, *Geophysical Research Letters*, *50*(17), doi:10.1029/2023GL102840. 1.3

Hersbach, H., B. Bell, P. Berrisford, G. Biavati, A. Horányi, J. M. Sabater, J. Nicolas, C. Peubey, R. Radu, I. Rozum, D. Schepers, A. Simmonds, C. Soci, D. Dee, and J.-N. Thépaut (2023), Era5 hourly data on single levels from 1940 to present, *Copernicus Climate Change Servise (C3S) Climate Data Store (CDS)*, doi:10.24381/cds.adbb2d47, accessed on 12-03-2024. 3.1

Heukamp, F. O., L. Aue, Q. Wang, M. Ionita, T. Kanzow, C. Wekerle, and A. Rinke (2023), Cyclones modulate the control of the north atlantic oscillation on transports

into the barents sea, *Communications Earth and Environment*, *4*(1), 324, doi:10.1038/s43247-023-00985-1. 1

Holton, J. (2004), *Introduction to Dynamic Meteorology*, 4 ed., Elsevier, Amsterdam. 2

Honda, M., J. Inoue, and S. Yamane (2009), Influence of low arctic sea-ice minima on anomalously cold eurasian winters, *Geophysical Research Letters*, *36*(8), doi:10.1029/2008GL037079. 5.2

Hoskins, B. J., and I. N. James (2014), *Fluid Dynamics of the Midlatitude Atmosphere*, 1 ed., John Wiley & Sons, Ltd., Hoboken. 2, 2, 3.3, 4.2.1

Inoue, J., and M. E. Hori (2011), Arctic cyclogenesis at the marginal ice zone: A contributory mechanism for the temperature amplification?, *Geophysical Research Letters*, *38*(12), doi:10.1029/2011GL047696. 5.1

Inoue, J., M. E. Hori, and K. Takaya (2012), The role of barents sea ice in the wintertime cyclone track and emergence of a warm-arctic cold-siberian anomaly, *Journal of Climate*, *25*(7), 2561–2569, doi:10.1175/JCLI-D-11-00449.1. 1.3

James, I. N. (1994), *Introduction to Circulating Atmospheres*, Cambridge Atmospheric and Space Science Series, Cambridge University Press, Cambridge. 2, 2

Koyama, T., J. Stroeve, J. Cassano, and A. Crawford (2017), Sea ice loss and arctic cyclone activity from 1979 to 2014, *Journal of Climate*, *30*(12), 4735–4754, doi:10.1175/JCLI-D-16-0542.1. 1.3

Lorenz, E. N. (1955), Available potential energy and the maintenance of the general circulation, *Tellus*, *7*(2), 157–167, doi:10.1111/j.2153-3490.1955.tb01148.x. 2

Madonna, E., C. Li, C. M. Grams, and T. Woollings (2017), The link between eddy-driven jet variability and weather regimes in the north atlantic-european sector, *Quarterly Journal of the Royal Meteorological Society*, *143*(708), 2960–2972, doi:10.1002/qj.3155. 1.2, 5.2

Madonna, E., G. Hes, C. Li, C. Michel, and P. Y. F. Siew (2020), Control of barents sea wintertime cyclone variability by large-scale atmospheric flow, *Geophysical Research Letters*, *47*(19), doi:10.1029/2020GL090322. 1, 1.2, 1.4, 2, 4.4.3

Markovsky, I., and S. Van Huffel (2007), Overview of total least-squares methods, *Signal Processing*, *87*(10), 2283–2302, doi:https://doi.org/10.1016/j.sigpro.2007.04.004, special Section: Total Least Squares and Errors-in-Variables Modeling. 4.2.2

Messori, G., C. Woods, and R. Caballero (2018), On the drivers of wintertime temperature extremes in the high arctic, *Journal of Climate*, *31*(4), 1597–1618, doi:10.1175/JCLI-D-17-0386.1. 1.2

Michel, C., A. Terpstra, and T. Spengler (2018), Polar mesoscale cyclone climatology for the nordic seas based on era-interim, *Journal of Climate*, *31*(6), 2511–2532, doi:10.1175/JCLI-D-16-0890.1. 3.2

Mooney, C. Z., and R. D. Duval (1993), *Bootstrapping: A nonparametric approach to statistical inference*, 95, Sage publications, doi:10.4135/9781412983532. 4.4

Mortin, J., G. Svensson, R. G. Graversen, M. L. Kapsch, J. C. Stroeve, and L. N. Boisvert (2016), Melt onset over arctic sea ice controlled by atmospheric moisture transport, *Geophysical Research Letters*, *43*(12), 6636–6642, doi:10.1002/2016GL069330. 1.2

Mrowiec, A. A., O. M. Pauluis, and F. Zhang (2016), Isentropic analysis of a simulated hurricane, *Journal of the Atmospheric Sciences*, *73*(5), 1857–1870, doi:10.1175/JAS-D-15-0063.1. 3.3, 3.4, 3.4

Murto, S., R. Caballero, G. Svensson, and L. Papritz (2022), Interaction between atlantic cyclones and eurasian atmospheric blocking drives warm extremes in the high arctic, *Weather and Climate Dynamics*, *3*(1), 21–44, doi:10.5194/wcd-2021-23. 5.2

Neu, U., M. G. Akperov, N. Bellenbaum, R. Benestad, R. Blender, R. Caballero, A. Cocozza, H. F. Dacre, Y. Feng, K. Fraedrich, J. Grieger, S. Gulev, J. Hanley, T. Hewson, M. Inatsu, K. Keay, S. F. Kew, I. Kindem, G. C. Leckebusch, M. L. Liberato, P. Lionello, I. I. Mokhov, J. G. Pinto, C. C. Raible, M. Reale, I. Rudeva, M. Schuster, I. Simmonds, M. Sinclair, M. Sprenger, N. D. Tilinina, I. F. Trigo, S. Ulbrich, U. Ulbrich, X. L. Wang, and H. Wernli (2013), Imilast: A community effort to intercompare extratropical cyclone detection and tracking algorithms, *Bulletin of the American Meteorological Society*, *94*(4), 529–547, doi:10.1175/BAMS-D-11-00154.1. 3.2

Papritz, L., and E. Dunn-Sigouin (2020), What configuration of the atmospheric circulation drives extreme net and total moisture transport into the arctic, *Geophysical Research Letters*, *47*(17), doi:10.1029/2020GL089769. 1.2, 2

Parker, D. J. (1998), Secondary frontal waves in the north atlantic region: A dynamical perspective of current ideas, *Quarterly Journal of the Royal Meteorological Society*, *124*(547), 829–856, doi:10.1002/qj.49712454709. 5.1

Pauluis, O., A. Czaja, and R. Korty (2008), The global atmospheric circulation on moist isentropes, *Science*, *321*(5892), 1075–1078, doi:10.1126/science.1159649. 3.4, 3.3

Pauluis, O. M., and A. A. Mrowiec (2013), Isentropic analysis of convective motions, *Journal of the Atmospheric Sciences*, *70*(11), 3673–3688, doi:10.1175/JAS-D-12-0205.1. 3.3, 3.4, 3.4, 3.4, 3.4, 4.2.4

Pinto, J. G., S. Zacharias, A. H. Fink, G. C. Leckebusch, and U. Ulbrich (2009), Factors contributing to the development of extreme north atlantic cyclones and their relationship with the nao, *Climate Dynamics*, *32*(5), 711–737, doi:10.1007/s00382-008-0396-4. 5.2

Priestley, M. D., J. G. Pinto, H. F. Dacre, and L. C. Shaffrey (2017), The role of cyclone clustering during the stormy winter of 2013/2014, *Weather*, *72*(7), 187–192, doi:10.1002/wea.3025. 1

Rinke, A., M. Maturilli, R. M. Graham, H. Matthes, D. Handorf, L. Cohen, S. R. Hudson, and J. C. Moore (2017), Extreme cyclone events in the arctic: Wintertime variability and trends, *Environmental Research Letters*, *12*(9), doi:10.1088/1748-9326/aa7def. 5.2

Serreze, M. C., and R. G. Barry (2005), *The Arctic Climate System*, Cambridge Atmospheric and Space Science Series, 1 ed., Cambridge University Press, Cambridge. 1.1, 1.1, 1.3, 2, 2, 5.1

Serreze, M. C., M. M. Holland, and J. Stroeve (2007), Perspectives on the arctic's shrinking sea-ice cover, *Science*, *315*, 1533–1536, doi:10.1126/science.1139426. 1.3

Shaw, T. A., M. Baldwin, E. A. Barnes, R. Caballero, C. I. Garfinkel, Y. T. Hwang, C. Li, P. A. O'Gorman, G. Rivière, I. R. Simpson, and A. Voigt (2016), Storm track processes and the opposing influences of climate change, *Nature Geoscience*, *9*(9), 656–664, doi:10.1038/ngeo2783. 1.2, 1.3

Simmonds, I., and R. J. Murray (1991a), A numerical scheme for tracking cyclone centres from digital data part i: development and operation of the scheme, *Australian Meteorological Magazine*, *39*, 155–166. 3.2

Simmonds, I., and R. J. Murray (1991b), A numerical scheme for tracking cyclone centres from digital data part ii: application to january and july general circulation model simulations, *Australian Meteorological Magazine*, *39*, 167–180. 3.2

Sorteberg, A., and B. Kvingedal (2006), Atmospheric forcing on the barents sea winter ice extent, *Journal of Climate*, *19*(19), 4772–4784, doi:10.1175/JCLI3885.1. 1.2

Sorteberg, A., and J. E. Walsh (2008), Seasonal cyclone variability at 70°n and its impact on moisture transport into the arctic, *Tellus, Series A: Dynamic Meteorology and Oceanography*, *60*(3), 570–586, doi:10.1111/j.1600-0870.2008.00314.x. 1

Stroeve, J., M. M. Holland, W. Meier, T. Scambos, and M. Serreze (2007), Arctic sea ice decline: Faster than forecast, *Geophysical Research Letters*, *34*(9), doi:10.1029/2007GL029703. 1, 1.3

Tao, D., C. Li, R. Davy, T. Spengler, C. Michel, and A. Rosendahl (2024), Thermodynamic variability of wintertime atlantic-arctic cyclones, *In preparation*. 1, 1.2, 1.4, 3.1

Tibaldi, S., A. Buzzi, and A. Speranza (1990), *Orographic Cyclogenesis*, pp. 107–127, American Meteorological Society, Boston, MA, doi:10.1007/978-1-944970-33-8_7. 5.1

UN DESA (2023), The sustainable development goals report 2023: Special edition, New York, UN DESA, https://unstats.un.org/sdgs/report/2023/. 1

Valkonen, E., J. Cassano, and E. Cassano (2021), Arctic cyclones and their interactions with the declining sea ice: A recent climatology, *Journal of Geophysical Research: Atmospheres*, *126*(12), doi:10.1029/2020JD034366. 4.4.2

Vallis, G. K. (2017), *Atmospheric and Oceanic Fluid Dynamics: Fundamentals and Large-Scale Circulation*, 2 ed., Cambridge University Press, Cambridge. 2, 2, 3.3, 3.4

Walker, E., D. Mitchell, and W. Seviour (2020), The numerous approaches to tracking extratropical cyclones and the challenges they present, *Weather*, *75*(11), 336–341, doi:10.1002/wea.3861. 3.2

Wallace, J. M., and P. V. Hobbs (2006), 1 - Introduction and Overview, in *Atmospheric Science (Second Edition)*, edited by J. M. Wallace and P. V. Hobbs, second edition ed., pp. 1–23, Academic Press, San Diego, doi:https://doi.org/10.1016/B978-0-12-732951-2.50006-5. 1

Wallace, J. M., P. V. Hobbs, L. McMurdie, and R. A. Houze (2006), 8 - Weather Systems, in *Atmospheric Science (Second Edition)*, edited by J. M. Wallace and P. V. Hobbs, second edition ed., pp. 313–373, Academic Press, San Diego, doi: https://doi.org/10.1016/B978-0-12-732951-2.50013-2. 1, 2, 2, 5.1

Walsh, J. E., D. H. Bromwich, J. E. Overland, M. C. Serreze, and K. R. Wood (2018), 100 years of progress in polar meteorology, *Meteorological Monographs*, *59*, 21.1–21.36, doi:10.1175/amsmonographs-d-18-0003.1. 1

Woollings, T., A. Hannachi, and B. Hoskins (2010), Variability of the north atlantic eddy-driven jet stream, *Quarterly Journal of the Royal Meteorological Society*, *136*(649), 856–868, doi:10.1002/qj.625. 5.2

Woollings, T., C. Li, M. Drouard, E. Dunn-Sigouin, K. A. Elmestekawy, M. Hell, B. Hoskins, C. Mbengue, M. Patterson, and T. Spengler (2023), The role of rossby waves in polar weather and climate, *Weather and Climate Dynamics*, *4*(1), 61–80, doi:10.5194/wcd-4-61-2023. 1